

Properties of ultra-compact particle-like solutions in Einstein-scalar-Gauss-Bonnet theories

Burkhard Kleihaus* and Jutta Kunz†

Institut für Physik, Universität Oldenburg, D-26111 Oldenburg, Germany

Panagiota Kanti‡

Division of Theoretical Physics, Department of Physics, University of Ioannina, GR-45110, Greece

(Dated: May 18, 2020)

Besides scalarized black holes and wormholes, Einstein-scalar-Gauss-Bonnet theories allow also for particle-like solutions. The scalar field of these particle-like solutions diverges at the origin, akin to the divergence of the Coulomb potential at the location of a charged particle. However, these particle-like solutions possess a globally regular metric, and their effective stress energy tensor is free from pathologies, as well. We determine the domain of existence for particle-like solutions in a number of Einstein-scalar-Gauss-Bonnet theories, considering dilatonic and power-law coupling functions, and we analyze the physical properties of the solutions. Interestingly, the solutions may possess pairs of lightrings, and thus represent ultra-compact objects. We determine the location of these lightrings, and study the effective potential for the occurrence of echoes in the gravitational-wave spectrum. We also address the relation of these particle-like solutions to the respective worm-hole and black-hole solutions, and clarify the limiting procedure to recover the Fisher solution (also known as Janis-Newman-Winicourt-Wyman solution).

I. INTRODUCTION

While our current experiments and observations are all in agreement with predictions of general relativity (GR), there are profound reasons to investigate alternative theories of gravity, that might represent low-energy effective theories, obtainable from some yet unknown fundamental theory of gravity (see e.g., [1–4]). One such class of attractive alternative theories of gravity is constituted by the so-called Einstein-scalar-Gauss-Bonnet (EsGB) theories. EsGB theories amend GR by including quadratic curvature terms, in the form of a topological invariant, the Gauss-Bonnet (GB) term, that is non-minimally coupled to a scalar field ϕ . These theories lead to second-order equations of motion, and do not suffer from the Ostrogradski instability or ghosts [5–7].

The EsGB action arises naturally in the framework of low-energy effective string theories, in which case the scalar field represents the dilaton [8–10]. The coupling function $F(\phi)$ is then of exponential type, $F(\phi) = \alpha \exp(-\gamma\phi)$, with coupling constants α and γ (and string theory value $\gamma = 1$). The black-hole solutions of the string-theory motivated EsGB action have been studied since a long time [11–27]. The EsGB equations of motion with this dilatonic coupling function do not allow for the Schwarzschild or Kerr solutions of GR. Instead, all these black holes carry dilatonic hair, evading the no hair theorem of GR (see e.g. [28, 29]) due to the presence of the GB term. Interestingly, the GB term also allows for dilatonic wormholes, since the GB term gives rise to an effective stress-energy tensor permitting the violation of the null energy condition (NEC) [30–32]. Unlike the wormholes in GR [33–40], these dilatonic wormholes do not need any type of exotic matter.

In recent years, EsGB theories with different coupling functions $F(\phi)$ moved into the focus of interest, when it was realized that an appropriately chosen coupling function would allow for curvature-induced spontaneous scalarization of black holes [41–43]. To allow for spontaneous scalarization, the GR black holes should remain solutions of the EsGB theories with a vanishing scalar field, and become unstable to the emergence of a non-trivial scalar field at some critical value(s) of the GB coupling strength [41–60], a mechanism reminiscent of matter-induced spontaneous scalarization in neutron stars [61]. The coupling function then needs a vanishing

*b.kleihaus@uni-oldenburg.de

†jutta.kunz@uni-oldenburg.de

‡pkanti@cc.uoi.gr

first derivative $dF/d\phi = 0$ for vanishing scalar field $\phi = 0$, and a positive second derivative. Other coupling functions will also allow for hairy black holes, albeit similar to the dilatonic case [41, 62–64]. As one might have expected, all these EsGB theories also allow for wormhole solutions without the presence of any exotic matter [65].

Black holes and wormholes represent highly compact objects which allow to scrutinize the effects of strong gravity predicted by GR and alternative theories of gravity, that give rise to distinct characteristic gravitational radiation in merger events observable by current and future gravitational-wave observatories (see e.g. [3, 66–68]). In particular, the presence of echoes in the ringdown may signal the absence of an event horizon in the final compact object [69–71]. Likewise, the shadows of highly compact objects may lead to distinctive observable effects depending significantly on the gravitational theory and on the type of *ultra-compact object* (UCO). Though current observations of the shadow of the supermassive black hole at the center of M87 are in agreement with the shadow being produced by a Kerr black hole [72], they still provide new observational bounds.

Recently, we have realized that EsGB theories possess another class of interesting compact objects, which represent particle-like solutions [73]. These static and spherically symmetric solutions possess a globally regular, asymptotically flat spacetime, but their scalar field diverges at the origin as r^{-1} . This is akin to the divergence of the Coulomb potential of a charged particle located at the origin. The effective stress-energy tensor of these particle-like solutions is everywhere regular, and yields simple expressions at the origin. Many of these particle-like solutions possess lightrings, and thus qualify as UCOs [71]. In fact, being horizonless, they always feature a pair of lightrings in agreement with general arguments [74]. The absence of a horizon also implies that these particle-like solutions will feature a sequence of echoes in a gravitational-wave signal [69–71].

Here, we provide a detailed discussion of these new particle-like solutions, considering EsGB theories for a set of coupling functions $F(\phi)$ of dilatonic and power-law type. We also allow for different boundary conditions of the scalar field at spatial infinity, yielding two distinct classes of solutions: those which possess an asymptotically vanishing scalar field, $\phi_\infty = 0$, and those that feature a finite asymptotic value of the scalar field, $\phi_\infty \neq 0$. A finite asymptotic value can be interpreted as a cosmological value, since it will subsist in solutions describing the evolution of the Universe. On the other hand, a vanishing asymptotic value in a theory with spontaneous scalarization will pass current constraints from binary mergers [75], since the scalar field may be set to zero in the cosmological context, yielding an evolution of the Universe in agreement with the standard cosmological Λ CDM model.

The structure of this paper is as follows: In section II we present the theoretical setting, including the action, the line-element and scalar-field ansatzes, and the equations of motion. We discuss the expansions at the origin and at infinity, including regularity of the effective stress-energy tensor and the curvature tensor, for the particle-like solutions, in section III. Here, we also discuss the limiting procedure that allows to recover the Fisher solution, also known as Janis-Newman-Winicourt-Wyman (JNWW) solution [76–80]. The numerical approach and the solutions themselves are presented in section IV. In section V, we present the domain of existence of the solutions, and address their relation to the black holes and wormholes of the respective theories. We discuss possible observational effects including lightrings and echoes in section VI, and we conclude in section VII.

II. THEORETICAL SETTING

We here consider the following effective action describing a class of EsGB theories,

$$S = \frac{1}{16\pi} \int d^4x \sqrt{-g} \left[R - \frac{1}{2} \partial_\mu \phi \partial^\mu \phi + F(\phi) R_{\text{GB}}^2 \right], \quad (1)$$

where R is the curvature scalar, ϕ is the scalar field with the coupling function $F(\phi)$, and

$$R_{\text{GB}}^2 = R_{\mu\nu\rho\sigma} R^{\mu\nu\rho\sigma} - 4R_{\mu\nu} R^{\mu\nu} + R^2 \quad (2)$$

is the quadratic Gauss-Bonnet correction term.

Variation of the action with respect to the metric and the scalar field leads to the Einstein equations and the scalar field equation,

$$G^\mu_\nu = T^\mu_\nu, \quad (3)$$

$$\nabla^\mu \nabla_\mu \phi + \dot{F}(\phi) R_{\text{GB}}^2 = 0 , \quad (4)$$

respectively, with the effective stress-energy tensor given by the expression

$$T_{\mu\nu} = -\frac{1}{4} g_{\mu\nu} \partial_\rho \phi \partial^\rho \phi + \frac{1}{2} \partial_\mu \phi \partial_\nu \phi - \frac{1}{2} (g_{\rho\mu} g_{\lambda\nu} + g_{\lambda\mu} g_{\rho\nu}) \eta^{\kappa\lambda\alpha\beta} \tilde{R}^{\rho\gamma}_{\alpha\beta} \nabla_\gamma \partial_\kappa F(\phi) . \quad (5)$$

Above, we have used the definitions $\tilde{R}^{\rho\gamma}_{\alpha\beta} = \eta^{\rho\gamma\sigma\tau} R_{\sigma\tau\alpha\beta}$ and $\eta^{\rho\gamma\sigma\tau} = \epsilon^{\rho\gamma\sigma\tau} / \sqrt{-g}$, and the dot denotes the derivative with respect to the scalar field ϕ .

To obtain static, spherically-symmetric solutions we assume the line-element in the form

$$ds^2 = -e^{f_0} dt^2 + e^{f_1} [dr^2 + r^2 (d\theta^2 + \sin^2 \theta d\varphi^2)] , \quad (6)$$

where the metric functions f_0 and f_1 are functions of the isotropic radial coordinate r only. We also assume that the scalar field ϕ depends only on r .

Substitution of the ansatz for the metric and the scalar field into the Einstein and scalar-field equations yields four coupled, nonlinear, ordinary differential equations, where three of them are of second order and one is of first order,

$$0 = \dot{F} [\phi' (f_1'^3 r^2 - 4f_1' f_1'' r^2 - 8f_1' - 8f_1'' r) - 2\phi'' (f_1'^2 r^2 + 4f_1' r)] / (2e^{2f_1} r^2) - \ddot{F} f_1' \phi'^2 [f_1' r + 4] / (e^{2f_1} r) + (f_1'^2 r + 8f_1' + 4f_1'' r + \phi'^2 r) / (4e^{f_1} r) , \quad (7)$$

$$0 = \dot{F} f_0' \phi' [-3f_1'^2 r^2 - 12f_1' r - 8] / (2e^{2f_1} r^2) + (2f_0' f_1' r + 4f_0' + f_1'^2 r + 4f_1' - \phi'^2 r) / (4e^{f_1} r) , \quad (8)$$

$$0 = -\dot{F} [\phi' (f_0'^2 f_1' r + 2f_0'^2 - 2f_0' f_1'^2 r - 2f_0' f_1' + 2f_0' f_1'' + 2f_0'' f_1' + 4f_0'') + \phi'' (2f_0' f_1' r + 4f_0')] / (2e^{2f_1} r) - \ddot{F} f_0' \phi'^2 [f_1' r + 2] / (e^{2f_1} r) + (f_0'^2 r + 2f_0' + 2f_0'' r + 2f_1' + 2f_1'' r + \phi'^2 r) / (4e^{f_1} r) , \quad (9)$$

$$0 = \dot{F} [f_0'^2 f_1'^2 r^2 + 4f_0'^2 f_1' r - f_0' f_1'^3 r^2 + 4f_0' f_1' f_1'' r^2 + 8f_0' f_1' + 8f_0' f_1'' r + 2f_0'' f_1'^2 r^2 + 8f_0'' f_1' r] / (2e^{2f_1} r^2) + (f_0' \phi' r + f_1' \phi' r + 4\phi' + 2\phi'' r) / (2e^{f_1} r) . \quad (10)$$

Equation (9) is now used to eliminate the second derivative f_0'' in Eq. (10). Also, Eq. (8) is used to eliminate f_0' in Eq. (10). Thus, we end up with a first-order equation for the function f_0 , and two second-order equations for the functions f_1 and ϕ of the form

$$Q_{11} f_1'' + Q_{12} \phi'' - P_1 = 0 , \quad Q_{21} f_1'' + Q_{22} \phi'' - P_2 = 0 , \quad (11)$$

where Q_{kl} and P_k depend on the functions f_1 and ϕ , and their first-order derivatives. Diagonalization of Eqs. (11) implies dividing by the determinant $\det Q$. If $\det Q$ possesses a node at some coordinate value r_\star , the respective solution of the equations of motion will no longer be regular but possess a cusp singularity at r_\star .

Furthermore, we note that the solutions are invariant under the scaling transformation

$$r \rightarrow \lambda r , \quad F \rightarrow \lambda^2 F , \quad \lambda > 0 . \quad (12)$$

III. EXPANSIONS AND REGULARITY

We now discuss the expansions at infinity and at the origin for the particle-like solutions of EsGB theories with various coupling functions, and we show regularity of their effective stress-energy tensor and of their curvature tensor. We then determine the redshift factor for these particle-like solutions, and address the possibility of a Smarr-like mass relation. We finally discuss the GR limit, where the Fisher (JNWW) solution, is recovered [76–80].

A. Expansion in the asymptotic region

Since we are interested in localised objects, we look for asymptotically-flat solutions described by power series expansions in $(1/r)$ in the asymptotic region $r \rightarrow \infty$. Our equations of motion then yield, up to order $\mathcal{O}(r^{-5})$,

$$f_0 = -\frac{2M}{r} - \frac{(D^2 + 4M^2)M}{24r^3} - 4\frac{\dot{F}_\infty D M}{r^4} + \mathcal{O}(r^{-5}) , \quad (13)$$

$$f_1 = \frac{2M}{r} - \frac{D^2 + 4M^2}{8r^2} + \frac{(D^2 + 4M^2)M}{24r^3} - \frac{(D^2 + 4M^2)^2 - 512\dot{F}_\infty DM}{256r^4} + \mathcal{O}(r^{-5}) , \quad (14)$$

$$\phi = \phi_\infty - \frac{D}{r} - \frac{(D^2 + 4M^2)D}{48r^3} - 4\frac{\dot{F}_\infty M^2}{r^4} + \mathcal{O}(r^{-5}) , \quad (15)$$

where $\dot{F}_\infty = \dot{F}(\phi_\infty)$. The constants M and D denote the mass and the scalar charge of the solutions, respectively. We note that the coefficients of all terms of higher-than-first order in r^{-1} are completely determined by the mass M , the scalar charge D and the asymptotic value of the scalar field ϕ_∞ .

B. Expansion at the origin

The expansion of the spacetime at the origin $r = 0$ is more involved. Here, we need to specify the coupling functions and exploit their explicit ϕ -dependence. Let us, therefore, restrict to polynomial coupling functions $F(\phi) = \alpha\phi^n$, with $n \geq 2$, and to dilatonic coupling functions $F(\phi) = \alpha e^{-\gamma\phi}$.

We first consider polynomial coupling functions, $F(\phi) = \alpha\phi^n$, with $n \geq 2$. We here assume a power series expansion for the metric functions, whereas for the scalar field we assume a behavior of the type

$$\phi = \phi_c - c_0/r + P_\phi(r) , \quad (16)$$

as $r \rightarrow 0$, where $P_\phi(r)$ is a polynomial in r . After substituting these expansions into the Einstein and scalar field equations, we can successively determine the expansion coefficients. We then find, that the lowest (non-zero) order in the expansion of the metric functions is exactly n , whereas it is $n-1$ in the expansion of the scalar-field polynomial $P_\phi(r)$. For general $n \geq 2$, we find

$$f_0 = f_{0c} + \frac{e^{f_{1c}}}{16\alpha n^2} (-c_0)^{(2-n)} r^n + \mathcal{O}(r^{n+1}) , \quad f_1 = f_{1c} + \frac{e^{f_{1c}}}{16\alpha n^2} (-c_0)^{(2-n)} r^n + \mathcal{O}(r^{n+1}) , \quad (17)$$

$$\phi = -\frac{c_0}{r} + \phi_c + \frac{5-2n}{n^2(n-1)} \frac{e^{f_{1c}}}{64\alpha} (-c_0)^{(3-n)} r^{(n-1)} + \mathcal{O}(r^n) . \quad (18)$$

Explicitly we find, for instance, for $n = 2$, the expansions

$$f_0 = f_{0c} + \frac{e^{f_{1c}}}{64\alpha} r^2 + \frac{e^{f_{1c}} \phi_c}{96\alpha c_0} r^3 + \mathcal{O}(r^4) , \quad (19)$$

$$f_1 = f_{1c} + \frac{e^{f_{1c}}}{64\alpha} r^2 + \frac{\nu_3}{6} r^3 + \mathcal{O}(r^4) , \quad (20)$$

$$\phi = -\frac{c_0}{r} + \phi_c - \frac{e^{f_{1c}} c_0}{256\alpha} r + \frac{32\alpha c_0 \nu_3 - e^{f_{1c}} \phi_c}{768\alpha} r^2 + \mathcal{O}(r^3) , \quad (21)$$

where f_{0c} , f_{1c} , ν_3 , ϕ_c , and c_0 are constants. The coefficients of all higher-order powers can be expressed in terms of these constants.

In the case of a dilatonic coupling function, $F(\phi) = \alpha e^{-\gamma\phi}$, a power-series expansion fails to lead to a local solution. Assuming $\gamma > 0$, we instead consider a non-analytic behaviour of the type

$$f_0 = f_{0c} + p_0(r) e^{-\gamma \frac{c_0}{r}} + \dots , \quad f_1 = f_{1c} + p_1(r) e^{-\gamma \frac{c_0}{r}} + \dots , \quad \phi = -\frac{c_0}{r} + \phi_c + p_\phi(r) e^{-\gamma \frac{c_0}{r}} + \dots , \quad (22)$$

where now $c_0 > 0$, $p_0(r)$, $p_1(r)$, and $p_\phi(r)$ are polynomials in r , and the dots indicate terms of order less than $e^{-\gamma \frac{c_0}{r}}$. Substitution into the Einstein and scalar-field equations then yields to lowest powers in $e^{-\gamma \frac{c_0}{r}}$ and r

$$f_0 = f_{0c} + \left(\frac{e^{f_{1c}}}{16\gamma^2 \alpha e^{-\gamma \phi_c}} \right) r^2 \left(1 - 2 \frac{r}{\gamma c_0} \right) e^{-\gamma \frac{c_0}{r}} , \quad (23)$$

$$f_1 = f_{1c} + \left(\frac{e^{f_{1c}}}{16\gamma^2 \alpha e^{-\gamma \phi_c}} + \nu_3 r \right) r^2 e^{-\gamma \frac{c_0}{r}} , \quad (24)$$

$$\phi = -\frac{c_0}{r} + \phi_c + c_0 \left[\frac{e^{f_{1c}}}{32\gamma^2 \alpha e^{-\gamma \phi_c}} \left(1 - \frac{3}{2} \frac{1}{\gamma c_0} r \right) + \frac{\nu_3}{2} r \right] r e^{-\gamma \frac{c_0}{r}} . \quad (25)$$

C. Stress-energy tensor and curvature tensor

We will now demonstrate the regularity of both the effective stress-energy tensor and curvature tensor at the origin $r = 0$. In order to find the effective stress-energy tensor at the origin, we substitute the respective expansions into the Einstein tensor and make use of the Einstein equations. For the polynomial coupling function with $n = 2$, we find, for the non-vanishing components of the effective stress-energy tensor, the results

$$T_t^t(0) = \frac{3}{32\alpha} , \quad T_r^r(0) = T_\theta^\theta(0) = T_\varphi^\varphi(0) = \frac{2}{32\alpha} . \quad (26)$$

Introducing the energy density $\epsilon_0 = -T_t^t(0)$ and the pressure $p_0 = T_r^r(0) = T_\theta^\theta(0) = T_\varphi^\varphi(0)$, the above expressions lead to a homogeneous equation of state $p_0(\epsilon_0) = -\frac{2}{3}\epsilon_0$ at the origin. It is interesting to note that the stress-energy tensor at the origin does not depend on the mass or the scalar charge. Also, the value of the energy density at the origin is not sign-definite and, in fact, is negative for positive coupling constant α . If instead we consider polynomial coupling functions with powers $n > 2$ or dilatonic coupling functions, then the stress-energy tensor vanishes identically at the origin, thus remaining again regular.

Let us now turn to the curvature invariants of the theory. If we substitute the expansions Eqs. (19)–(21) into the curvature invariants, for the polynomial coupling function with $n = 2$, we obtain the expressions

$$R(0) = -\frac{9}{32\alpha} , \quad R_{\mu\nu}R^{\mu\nu}(0) = \frac{21}{(32\alpha)^2} , \quad R_{\mu\nu\kappa\lambda}R^{\mu\nu\kappa\lambda}(0) = \frac{15}{(32\alpha)^2} , \quad R_{\text{GB}}^2 = \frac{12}{(32\alpha)^2} , \quad (27)$$

which again depend only on the coupling constant α . As was the case for the stress-energy tensor, the curvature invariants vanish at the origin for either polynomial coupling functions with powers $n > 2$ or for dilatonic coupling functions.

It is also straightforward to show that all components of the stress-energy tensor as well as all curvature invariants vanish at asymptotic infinity in accordance with the condition of asymptotic flatness. As we will demonstrate in the following sections, where complete numerical solutions are presented, our particle-like solutions are characterized by regularity not only at these two asymptotic regions but over the entire radial regime.

D. Redshift and Smarr-type mass relation

The redshift constitutes an interesting observable for compact objects. To obtain the redshift, we consider the ratio of the wavelength of a photon as measured by an observer in the asymptotic region, λ_{asym} , to the wavelength of the photon as emitted at the origin, λ_{emit} ,

$$\frac{\lambda_{\text{asym}}}{\lambda_{\text{emit}}} = \frac{\sqrt{-g_{tt}(\infty)}}{\sqrt{-g_{tt}(0)}} = e^{-f_0(0)/2} . \quad (28)$$

The corresponding redshift factor z is then given by

$$z = \frac{\lambda_{\text{asym}}}{\lambda_{\text{emit}}} - 1 = e^{-f_0(0)/2} - 1 . \quad (29)$$

For black holes and wormholes in dilatonic EsGB theories, Smarr-type mass relations are known to exist [16, 30]. In order to obtain analogously a Smarr-type mass relation for the particle-like solutions, we start from the Komar expression for the mass

$$M = \frac{1}{4\pi} \int_{\Sigma} R_{\mu\nu} \xi^\mu n^\nu dV = -\frac{1}{4\pi} \int_{\Sigma} R_t^t \sqrt{-g} d^3x . \quad (30)$$

In the above expression, $\xi^\mu = (1, 0, 0, 0)$ is the timelike Killing vector, $n^\nu = (e^{-f_0/2}, 0, 0, 0)$ is the unit vector normal to the spacelike hypersurface Σ , and dV the natural volume element on Σ . Making use of the equations of motion, we may write

$$R_t^t = T_t^t - \frac{1}{2} T_\mu^\mu = \frac{1}{2} (T_t^t - T_r^r - 2T_\theta^\theta) + \lambda \left[\nabla^\mu \nabla_\mu \phi + \dot{F}(\phi) R_{GB}^2 \right] , \quad (31)$$

where, as a last term, we have added a zero in the form of the scalar-field equation multiplied by a real constant λ . If we also multiply the above by $\sqrt{-g}$, we write

$$\sqrt{-g} R_t^t = \sqrt{-g} \left[\frac{1}{2} (T_t^t - T_r^r - 2T_\theta^\theta) + \lambda \dot{F}(\phi) R_{GB}^2 \right] + \lambda \partial_\mu (\sqrt{-g} \partial^\mu \phi), \quad (32)$$

or, if we use the explicit expressions for the T_ν^μ components and the GB term,

$$\begin{aligned} \sqrt{-g} R_t^t = & -2 \sin \theta \partial_r \left\{ e^{(f_0 - f_1)/2} r \left[f_1' \left(1 + \frac{f_1' r}{4} \right) (F f_0' - F') + F' f_0' \left(1 + \frac{f_1' r}{2} \right) - \frac{\lambda}{2} e^{f_1} \phi' r \right] \right\} \\ & + (F + 2\lambda \dot{F}) \partial_r \left[e^{(f_0 - f_1)/2} r f_0' f_1' \left(1 + \frac{f_1' r}{4} \right) \right]. \end{aligned} \quad (33)$$

For a nontrivial coupling function $F(\phi)$, the last term in the above expression prevents us from writing $\sqrt{-g} R_t^t$ in the form of a total derivative with respect to the radial coordinate. If, however, it holds that $F + 2\lambda \dot{F} = 0$, i.e. if $F(\phi) = \alpha e^{-\gamma \phi}$ with $\gamma = 1/2\lambda$, the last term in Eq. (33) vanishes. Then, employing the expansions for the metric functions and the scalar field at infinity and at the origin, the integral over the volume in Eq. (30) leads to the relation

$$M + \frac{D}{2\gamma} = e^{\frac{f_{0c} + f_{1c}}{2}} \frac{c_0}{4\gamma} (1 - 8\alpha c_0 \nu_3 \gamma^3 e^{-f_{1c}} e^{-\gamma \phi_c}). \quad (34)$$

The above Smarr-type formula combines the global charges of the particle-like solutions obtained at infinity, the mass M and the scalar charge D , with an expression of the fields evaluated at the origin. The latter here replaces the contributions from the horizon in the case of black holes and the throat in the case of wormholes. As in the case of the aforementioned studies, a non-integral, closed-form for the Smarr-type relation can be derived only in the case of the dilatonic coupling function.

E. GR limit

For a constant GB coupling function, the EsGB theory reduces to GR with a self-gravitating scalar field. In this limit, a singular solution is known in closed form, the Fisher (JNWW) solution [76–80]. In terms of the metric (6) with isotropic coordinates, this solution reads

$$e^{f_0} = \left(\frac{1 - r_s/r}{1 + r_s/r} \right)^{2s}, \quad e^{f_1} = (1 - r_s^2/r^2)^2 e^{-f_0}, \quad \phi = \phi_\infty \pm \frac{d}{2} f_0, \quad (35)$$

where $d = D/M$ is the scaled scalar charge, and $s = 1/\sqrt{1 + d^2/4}$. The curvature singularity is located at $r_s = M/2s$. In the limit $d \rightarrow 0$, corresponding to $s \rightarrow 1$, the Schwarzschild solution is obtained. Note that in this limit $\phi = \phi_\infty$.

Let us now address the relation between the particle-like EsGB solutions and the Fisher solution. We note that in the limit $d \rightarrow \infty$ the scale symmetry, Eq. (12), of the field equations implies that the mass, the scalar charge, and the coupling strength scale as

$$M \rightarrow \lambda M, \quad D \rightarrow \lambda D, \quad \alpha \rightarrow \lambda^2 \alpha. \quad (36)$$

By scaling with a factor $\lambda = 1/D$, we can achieve that the coupling functions vanish in this limit. We are then left with a solution for a self-gravitating scalar field in GR. Solutions with $M = 0$ exist in closed form

$$e^{f_0} = 1, \quad e^{f_1} = \left(\frac{1 - \frac{D}{4r}}{1 + \frac{D}{4r}} \right)^2, \quad \phi = \phi_\infty + f_1, \quad (37)$$

which possess a curvature singularity at $r = D/4$.

This solution can be obtained from the Fisher solution (35) by taking the limit $d \rightarrow \infty$ while keeping r_s fixed. This implies taking the limit $s \rightarrow 0$ while keeping fixed $s d$. Similarly, by fixing d and taking the limit $\hat{\alpha} \rightarrow 0$, where $\hat{\alpha} = 8\alpha/M^2$, we see that the particle-like solutions tend to the Fisher solution, when the radial coordinate r is larger than the value of the radial coordinate of the Fisher singularity, i.e. $r > r_s$. In the interval $0 \leq r \leq r_s$ the metric components g_{tt} and g_{rr} tend to zero, leading again to a singular region.

IV. NUMERICAL APPROACH AND SOLUTIONS

We turn now to our numerical analysis. We first discuss the numerical approach used in constructing the particle-like solutions. Then, we present a set of solutions, construct their embedding diagrams, illustrate the cusp singularity and indicate the GR limit.

A. Numerical approach

In order to solve numerically the set of the second-order ordinary differential equations given in Eqs. (11), we introduce the new coordinate

$$\xi = \frac{r_0}{r}, \quad (38)$$

where the constant r_0 is a scaling parameter. We also rescale the coupling constant $\alpha \rightarrow \alpha r_0^2$. Then, all the differential equations are independent of the parameter r_0 .

In terms of the new coordinate ξ , the asymptotic expansions (13)-(15) read

$$f_0 \rightarrow -2M\xi + \mathcal{O}(\xi^2), \quad f_1 \rightarrow 2M\xi + \mathcal{O}(\xi^2), \quad \phi \rightarrow \phi_\infty - D\xi + \mathcal{O}(\xi^2), \quad (39)$$

where M and D have also been rescaled, i. e. $M \rightarrow r_0 M$, $D \rightarrow r_0 D$. We recall that the coefficients of all higher order terms in ξ can be expressed in terms of the three constants M , D and ϕ_∞ . Thus, for a given coupling function, the solutions are then completely determined by these three parameters.

We treat the set of ordinary differential equations as an initial value problem, for which we employ the fourth order Runge Kutta method. The initial values for the functions follow immediately from the expansion (39)

$$f_{0 \text{ ini}} = 0, \quad f_{1 \text{ ini}} = 0, \quad \frac{df_1}{d\xi}_{\text{ini}} = 2M, \quad \phi_{\text{ini}} = \phi_\infty, \quad \frac{d\phi}{d\xi}_{\text{ini}} = -D. \quad (40)$$

We perform the numerical calculations in the interval $\xi_{\min} \leq \xi \leq \xi_{\max}$, choosing always the lower bound $\xi_{\min} = 10^{-8}$. On the other hand, for the upper bound we choose $\xi_{\max} = 100$ in the case of the quadratic coupling function, and $\xi_{\max} = 10$ in the case of the dilatonic coupling function.

B. Numerical solutions

We now present typical sets of particle-like solutions. Figure 1 shows the metric functions $-g_{tt}$ (first row) and g_{rr} (second row) as well as the scalar-field function ϕ (third row) versus the scaled radial coordinate $\hat{r} = r/M$ for the coupling functions $F = \alpha\phi^2$ with $\phi_\infty = 0$ (left column) and $F = \alpha e^{-\phi}$ (right column; for the needs of our numerical analysis, we will henceforth set $\gamma = 1$). Each graph presents several solutions for different values of the scaled GB coupling constant $\hat{\alpha} = 8\alpha/M^2$ and the scaled scalar charge $d = D/M$.

Figure 1 clearly demonstrates the regularity of the metric at the origin $r = 0$, where the metric functions assume finite values, in full agreement with the expansions. In the same regime, the scalar field is shown to diverge in accordance again with its asymptotic expansions found in the previous Section. At large distances, both metric functions obey the asymptotic flatness condition whereas the scalar field assumes a constant, vanishing value.

The behaviour of the metric tensor and scalar field near the origin $r = 0$ is more clearly depicted in Fig. 2. The finite asymptotic values of the two metric components $-g_{tt}$ and g_{rr} at the origin are shown in the first and second row, respectively, for numerous sets of solutions in order to illustrate their dependence on the GB coupling constant. Also shown is the coefficient c_0 of the diverging term in the expansion of the scalar field at the origin, for the same set of solutions. The two columns correspond again to the two choices for the coupling function, namely the quadratic and the exponential function.

In Fig. 3, we depict two scalar invariant quantities, the scalar curvature R (indicated by solid lines) and the Gauss-Bonnet term (indicated by dashed lines) in terms of the scaled radial coordinate \hat{r} . Their profiles are presented for a number of solutions corresponding to different values of the parameters $\hat{\alpha}$ and d , and clearly

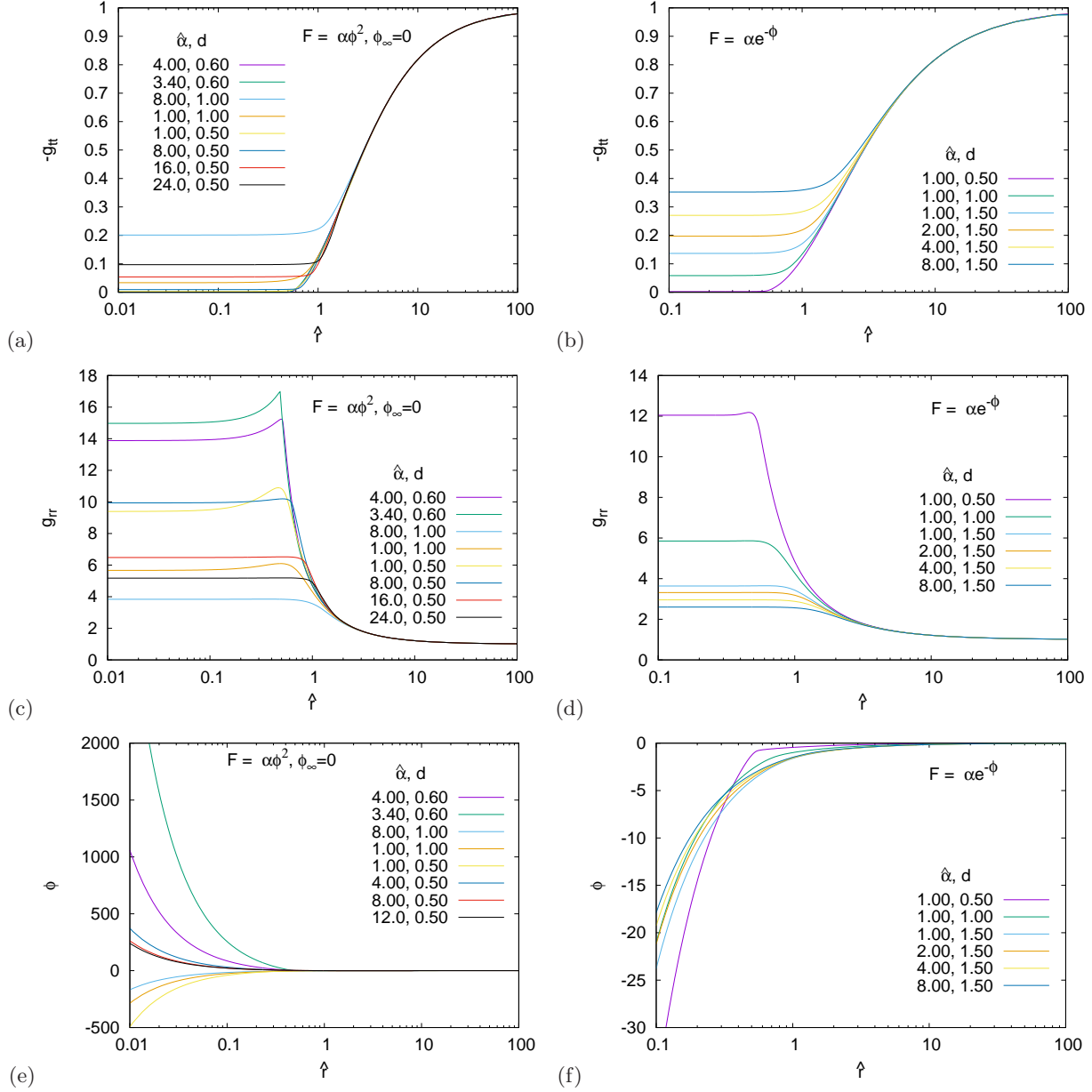


FIG. 1: (a)-(f) The metric functions $-g_{tt}$ and g_{rr} and the scalar field ϕ vs the scaled radial coordinate \hat{r} for the coupling functions $F = \alpha\phi^2$ with $\phi_\infty = 0$ [left column: (a), (c), (e)] and $F = \alpha e^{-\phi}$ [right column: (b), (d), (f)] for several values of $\hat{\alpha}$ and d .

demonstrate the regularity of spacetime. Both curvature invariants assume finite asymptotic values near the origin $r = 0$, reach their maximum values at some small value of \hat{r} (where the stress-energy tensor T^μ_ν also reaches its maximum value, as we will later see) and vanish at asymptotic infinity.

As we observe in Fig. 1, the metric function g_{tt} is always monotonic. However, this is not always the case for the metric function g_{rr} . Depending on the parameters, the metric function g_{rr} may exhibit a maximum away from the origin and then fall sharply with increasing radial coordinate. This behavior entails that the relation

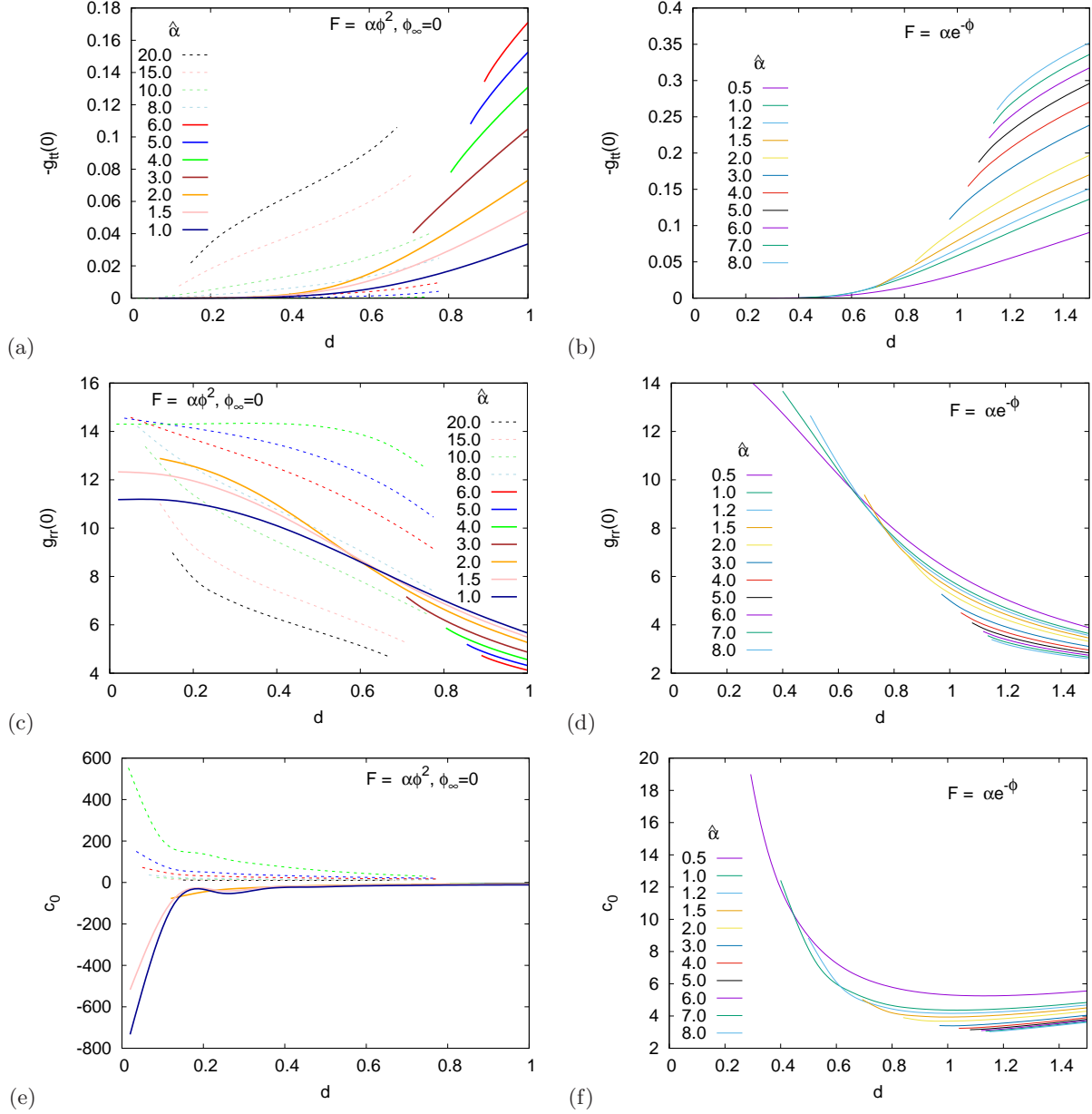


FIG. 2: (a)-(f) The value of the metric components $-g_{tt}(0)$ and $g_{rr}(0)$ at the origin, and the coefficient c_0 of the diverging term in the expansion of the scalar field ϕ at the origin vs the scaled scalar charge d for the coupling functions $F = \alpha\phi^2$ with $\phi_\infty = 0$ [left column: (a), (c), (e)] and $F = \alpha e^{-\phi}$ [right column: (b), (d), (f)] for several values of $\hat{\alpha}$. (The values of $\hat{\alpha}$ in (e) are the same as in (a) and (c))

between the radial coordinate r and the circumferential coordinate R_c , defined as

$$R_c = \frac{1}{2\pi} \int_0^{2\pi} \sqrt{g_{\varphi\varphi}}|_{\theta=\pi/2} d\varphi = r e^{f_1/2}, \quad (41)$$

may not be monotonic any more, and this may have interesting consequences for the geometry of the spacetime: The circumferential radius $R_c(r)$ in that case features a local maximum and a local minimum, where the local

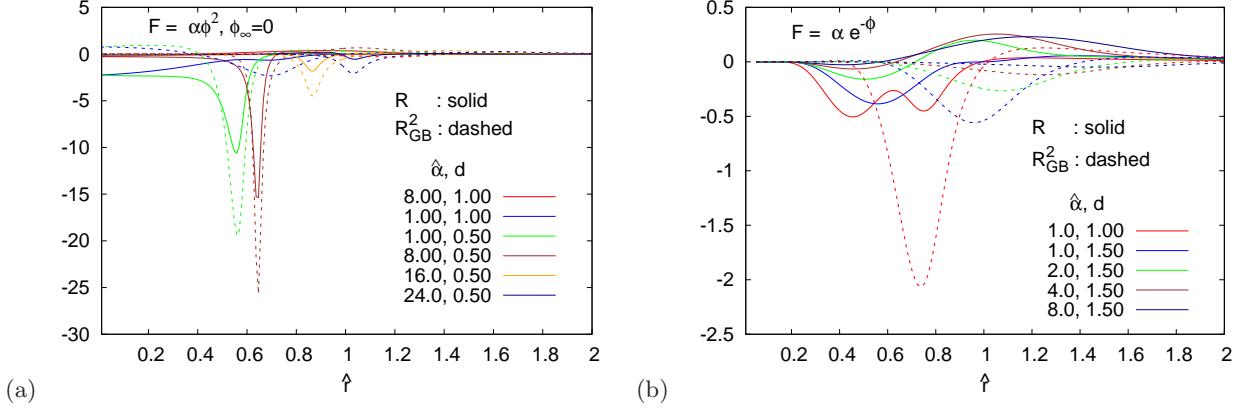


FIG. 3: The scalar curvature R (solid lines) and Gauss-Bonnet term R_{GB}^2 (dashed lines) vs the scaled radial coordinate \hat{r} for the coupling functions (a) $F = \alpha\phi^2$ with $\phi_\infty = 0$, and (b) $F = \alpha e^{-\phi}$, and for several values of $\hat{\alpha}$ and d .

minimum corresponds to a throat while the local maximum represents an equator.

C. Embedding diagrams

Let us now visualize the spatial geometry of these particle-like solutions, by illustrating the dependence of their circumferential coordinate $R_c(r)$ on the radial coordinate and by embedding these solutions into Euclidean space. In particular, we take the line-element of our solutions Eq. (6) at $t = \text{const.}$ and $\theta = \pi/2$, and set it equal to the line-element of the three-dimensional Euclidean space

$$e^{f_1} (dr^2 + r^2 d\varphi^2) = d\rho^2 + \rho^2 d\varphi^2 + dZ^2, \quad (42)$$

where ρ , φ and Z are the Euclidean coordinates. We then consider r and Z as functions of ρ . Identifying $\rho = r e^{f_1/2}$ from the $g_{\varphi\varphi}$ terms, we obtain Z via the integral

$$Z(\rho) = \pm \int_0^\rho \sqrt{\left(\frac{dr}{d\tilde{\rho}}\right)^2 e^{f_1(\tilde{\rho})} - 1} d\tilde{\rho}. \quad (43)$$

This then gives us a parametric representation of the embedded ($\theta = \pi/2$)-plane for a fixed value of the φ coordinate. The geometry of the particle-like solutions is then visualized by considering the respective surface of revolution.

Figure 4 shows the circumferential coordinate $R_c(r)$, Eq. (41), for the same sets of solutions as those in Fig. 1, and the embedding relation $Z(\rho)$, Eq. (43). In particular, in Fig. 4(c) we notice, that the geometry can develop a throat and an equator. However, in contrast to wormhole solutions [65], the second asymptotic infinity is missing in these particle-like spacetimes, since the origin is a regular point. We note that regular solutions with a throat and an equator have also been obtained in different contexts [81–84].

We demonstrate the wide variety of different geometries in Fig. 5, for a set of particle-like solutions with a quadratic coupling function and an asymptotically vanishing scalar field. In Figs. 5(a)-(d), we see a typical particle-like solution, a solution with a throat and an equator, a solution with a degenerate throat and an excited solution (emerging for large values of $\hat{\alpha}$, as discussed in Sec. V), respectively. For a dilatonic coupling function, on the other hand, we do not find solutions featuring a throat and an equator. The presence or absence of such solutions will be reflected in the domain of existence of the particle-like solutions, which is discussed in the next section.

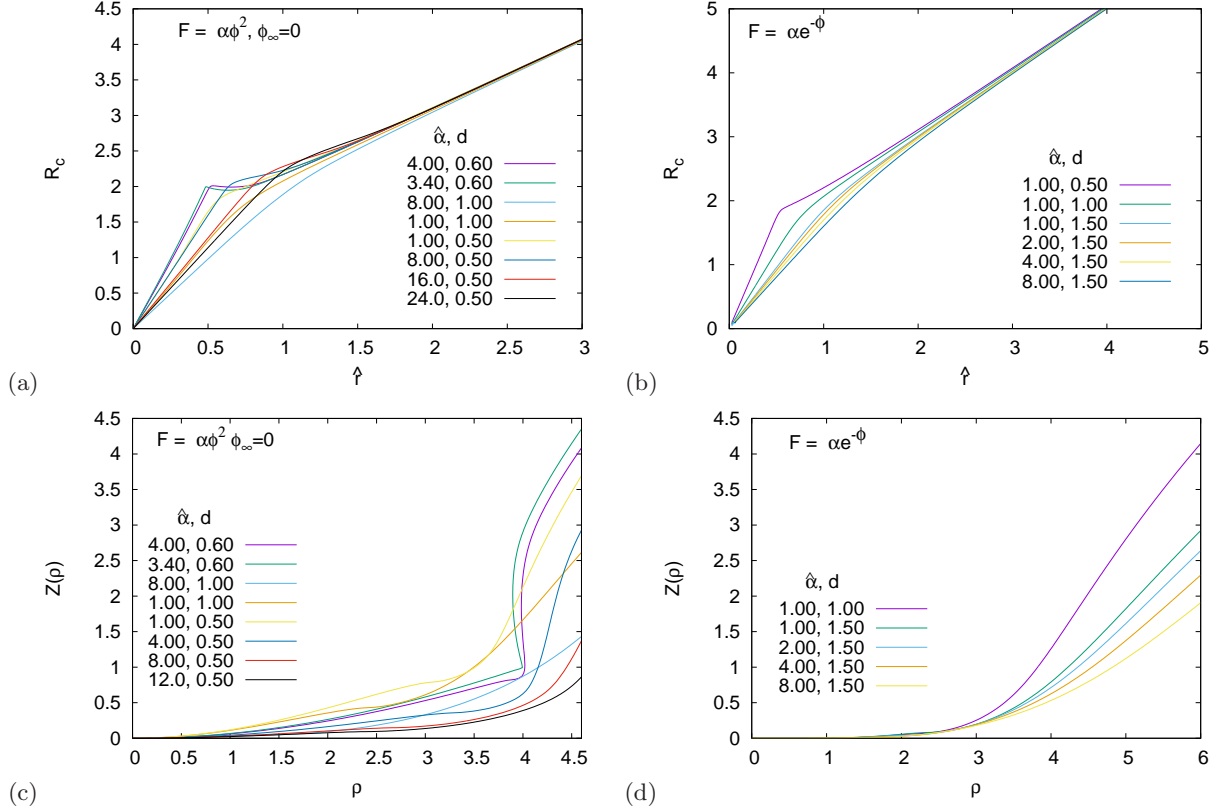


FIG. 4: (a)-(d) The circumferential coordinate $R_c(r)$ and the embedding relation $Z(\rho)$ for the coupling functions $F = \alpha\phi^2$ with $\phi_\infty = 0$ [left column: (a), (c)] and $F = \alpha e^{-\phi}$ [right column: (b), (d)] for several values of $\hat{\alpha}$ and d .

D. Cusp singularity

As noted in Section II, for the numerical procedure we need to diagonalize the second-order differential equations with respect to the second derivatives of the metric function f_1 and the scalar-field function ϕ . This then introduces the determinant of the matrix of coefficients $\det Q$ in the denominator of the diagonalized equations. When this determinant develops a node at some coordinate value r_* , this leads to a cusp singularity in the respective solution.

In Fig. 6, we demonstrate how such a cusp singularity forms. For that purpose, we exhibit the metric function f_1 , its first derivative $f_{1,r}$ and its second derivative $f_{1,rr}$ for a family of solutions for the coupling function $F = a\phi^2$ with $\phi_\infty = 0$ for $\hat{\alpha} = 0.5$ and varying scalar charge d , approaching the critical charge d_c of the solution with the cusp singularity. We note that we find two types of cusp singularities. In type (i), the second derivative $f_{1,rr}$ (and likewise ϕ_{rr}) develops a jump at a critical r_* [left column: (a), (c), (e)]. Here, the denominator behaves as $(r - r_*)$. In type (ii), $f_{1,rr}$ diverges at r_* [right column: (b), (d), (f)]. Here, the denominator behaves as $(r - r_*)^g$ with $g < 1$. In our numerical procedure, we monitor the determinant and stop the computation if this quantity changes sign.

E. GR limit

We demonstrate in Fig. 7 how the particle-like solutions change as the limiting GR solution, i.e., the Fisher (or JNWW) solution, is approached. Here, the coupling function is $F = \alpha\phi^2$ with $\phi_\infty = 0$. The functions of

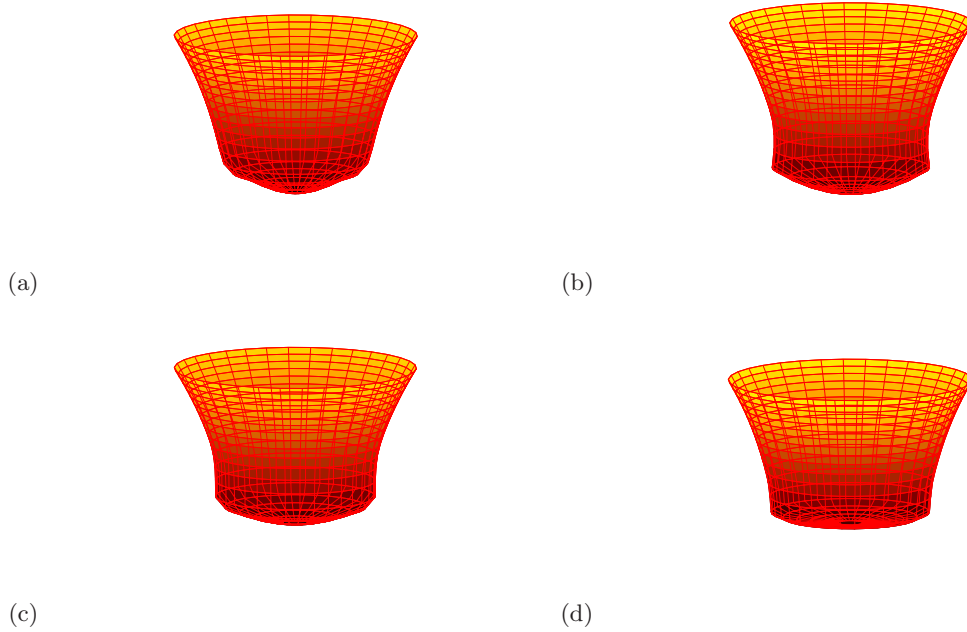


FIG. 5: The isometric embedding of the equatorial plane for particle-like solutions for the coupling function $F = a\phi^2$ with $\phi_\infty = 0$ for: (a) $\hat{\alpha} = 1, d = 0.5$; (b) $\hat{\alpha} = 3.4, d = 0.6$; (c) $\hat{\alpha} = 4.68, d = 0.6$; (d) $\hat{\alpha} = 28, d = 0.15$.

the GR solution are indicated by dotted lines, while the location of its curvature singularity is marked by the vertical line. As predicted in Sec. II, in the exterior region $r > r_s$, all functions of the particle-like solutions indeed tend towards the corresponding functions of the GR solutions, while, in the interior region $r < r_s$, the metric functions tend to zero, leading to a singular interior region.

V. DOMAIN OF EXISTENCE

We now present the domain of existence of the particle-like EsGB solutions considering, in particular, quadratic, cubic and dilatonic coupling functions. We also address their relation to the black holes and worm-holes of the respective theories.

A. Quadratic EsGB solutions

We begin by investigating the domain of existence of the quadratic EsGB solutions. The coupling function $F = \alpha\phi^2$ is symmetric in ϕ , and thus the solutions come in degenerate pairs with respect to the transformation $\phi \rightarrow -\phi$, carrying positive and negative scalar charge, provided the symmetry is respected by the boundary conditions as dictated by the choice of $\phi_\infty = 0$. To inspect the domain of existence it is therefore sufficient to restrict to non-negative scalar charge d .

We exhibit the domain of existence in Figs. 8(a) and (b) for $\phi_\infty = 0$, employing the scalar charge d and the scaled GB coupling constant $\hat{\alpha}$ to delimit its size. We restrict to $\hat{\alpha} \geq 0$. As we see in Fig. 8(a), for a quadratic coupling function, the domain of existence consists of many disconnected regions due to the emergence of solutions with a radially excited scalar field for large values of $\hat{\alpha}$. In these figures, all regions with particle-like solutions are shown in blue color.

Figure 8(b) provides a magnification of the domain of existence up to the value $\hat{\alpha} = 6$, and allows one to observe more carefully the different regions. The lowest region, corresponding to small values of $\hat{\alpha}$, contains particle-like solutions without nodes of the scalar field. Here, ϕ is negative as it approaches the origin. In the

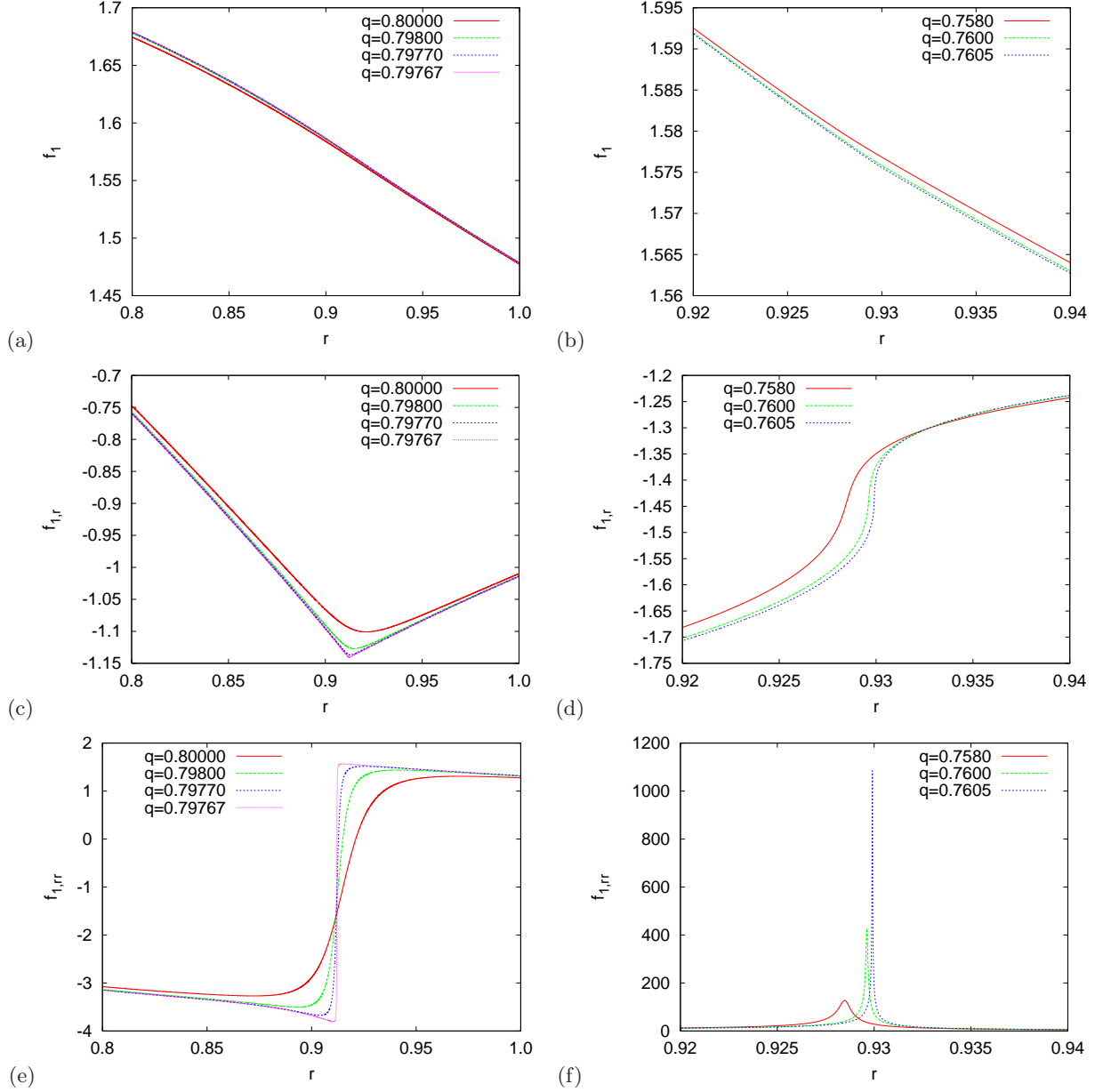


FIG. 6: (a)-(f) The emergence of a cusp singularity for the function f_1 in a family of solutions for the coupling function $F = a\phi^2$ with $\phi_\infty = 0$ for $\hat{\alpha} = 0.5$ and varying scalar charge d . In type (i), the second derivative $f_{1,rr}$ develops a jump at a critical r_* [left column: (a), (c), (e)], whereas in type (ii), $f_{1,rr}$ diverges at r_* [right column: (b), (d), (f)].

second region, located above and to the left of the first region, there are particle-like solutions with one node. Here, ϕ is positive as it approaches the origin. Parts of these regions, both indicated by blue colour, are seen in Figs. 8(a)-(b). In Fig. 8(a), also part of the third region is seen, where the scalar field has two nodes and is again negative as it approaches the origin. The regions with more nodes reside at still higher values of $\hat{\alpha}$.

Let us now inspect the boundaries of the domain of existence. There are various mechanisms that delimit the domain. The nodeless particle-like solutions are simply delimited by the occurrence of a cusp singularity, marked by a dark blue line. The excited particle-like solutions are also delimited by singular solutions, where

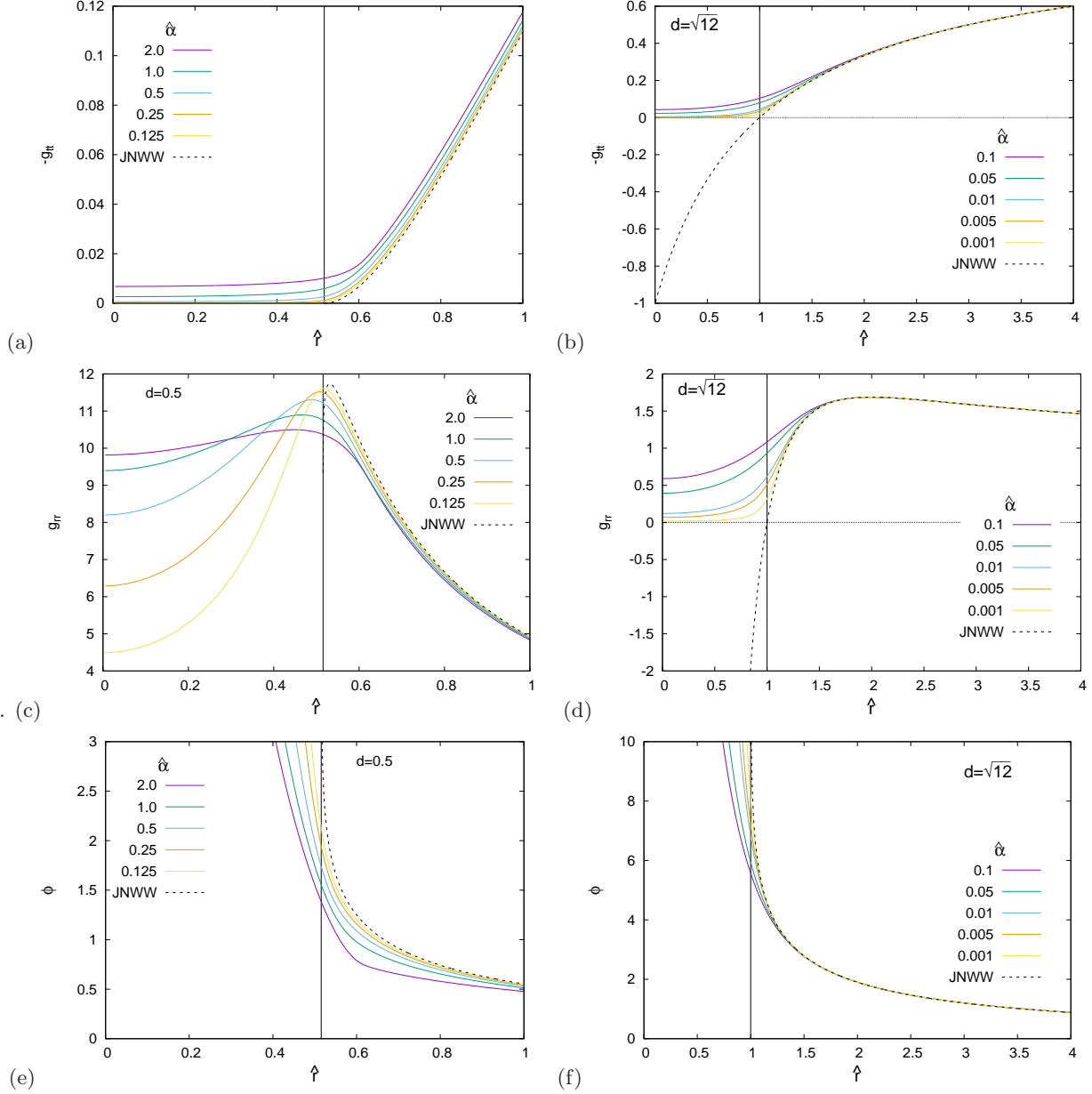


FIG. 7: (a)-(f) The metric functions $-g_{tt}$ and g_{rr} and the scalar field ϕ vs the scaled radial coordinate \hat{r} for the coupling function $F = \alpha\phi^2$ with $\phi_\infty = 0$ in the GR limit $\hat{\alpha} \rightarrow 0$ for scaled dilaton charge $d = 1/2$ [left column: (a), (c), (e)] and $d = \sqrt{12}$ [right column: (b), (d), (f)]. The limiting Fisher (JNWW) solution is also indicated (dotted) together with the location of its curvature singularity (vertical line).

g_{tt} vanishes at some point. These are marked by a red line. The excited particle-like solutions possess regions of overlap with the wormhole solutions, indicated by a darker shade of blue. In these regions, the particle-like solutions possess a throat and an equator. In this overlapping region, wormholes can be constructed from the particle-like solutions by either cutting at the throat or cutting at the equator, and then continuing (after a suitable coordinate transformation) with the symmetrically reflected solution into the second asymptotic region. Let us note that wormholes can also be constructed from singular solutions with throat/equator in the case

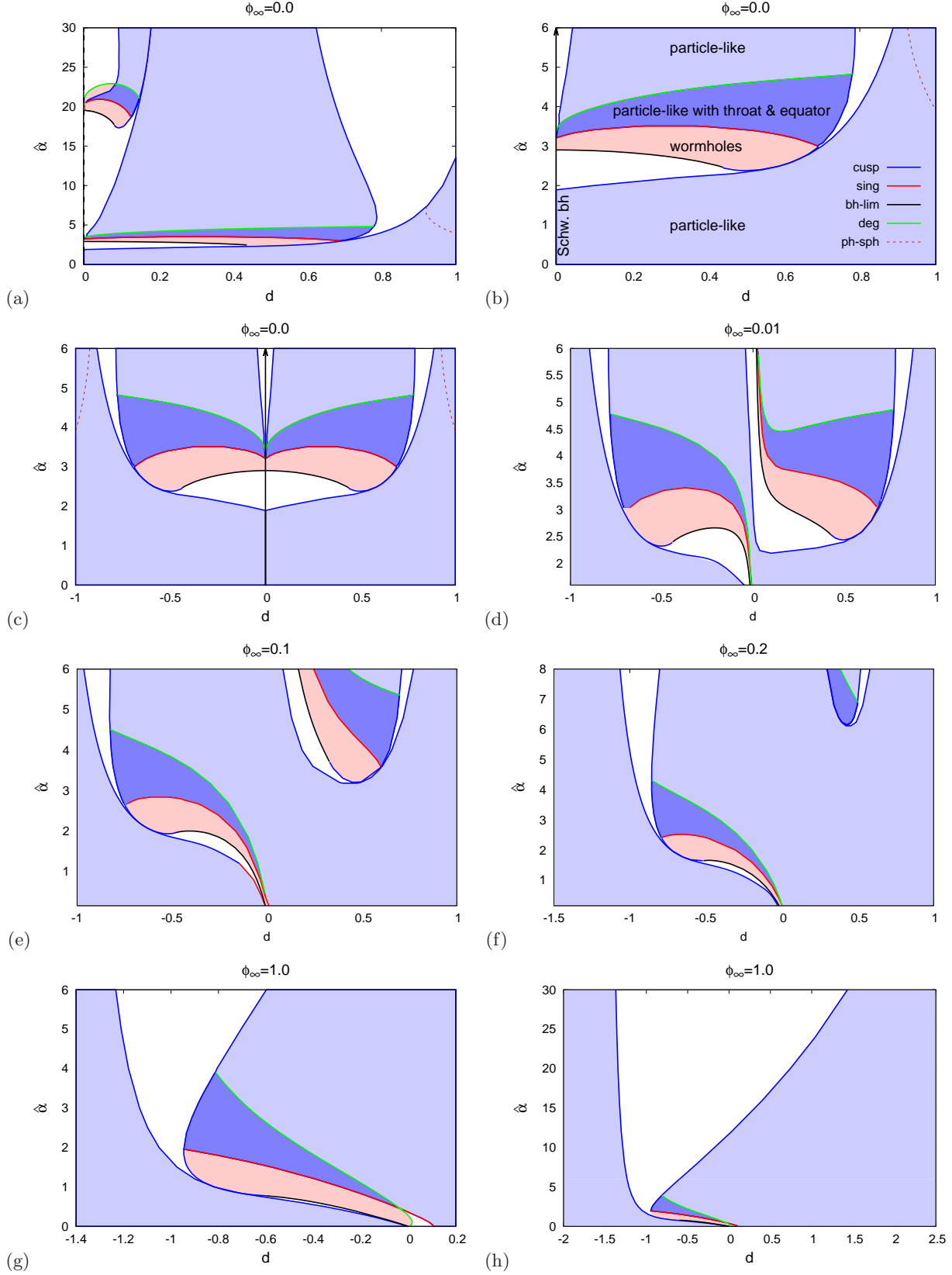


FIG. 8: Domain of existence (blue) in the $d - \hat{\alpha}$ plane for the quadratic coupling function $F = \alpha \phi^2$ with $\phi_\infty = 0$ (a), (b) and (c), and for $\phi_\infty = 0.01$ (d), $\phi_\infty = 0.1$ (e), $\phi_\infty = 0.2$ (f), $\phi_\infty = 1$ (g) and (h). Also included are the domains of existence of wormholes (dark-blue and rose) and black holes (black curves). The boundaries of the domain of existence are marked differently for cusp singularities (blue) and curvature singularities (red). The green curves show solutions with degenerate throat. The domain with both particle-like objects and wormholes is indicated in dark blue. The domain with wormholes only (rose) is in part delimited by scalarized black holes. The dashed curve indicates the boundary of solutions for which lightrings exist. Solutions without lightrings are located above and to the right of the dashed curve.

that the singularity is located at a smaller radius than the one of the throat/equator. The limiting line of the overlap region of particle-like and wormhole solutions to the region with particle-like solutions only is marked in green. The region with wormholes only is shown in rose. The vertical line (at the value $d = 0$) represents the Schwarzschild black holes. The location of the fundamental branch of the scalarized EsGB black holes is indicated in black, and likewise the location of the first excited EsGB black hole branch in Fig. 8(a).

When we allow for a non-vanishing value of the scalar field at infinity, $\phi_\infty \neq 0$, the symmetry is broken, and we have to study both positive and negative values of the scalar charge. In Figs. 8(c)-(h), we illustrate how the domain of existence changes as the asymptotic value ϕ_∞ increases. In particular, we choose $\phi_\infty = 0$ [Fig. 8(c)], $\phi_\infty = 0.01$ [Fig. 8(d)], $\phi_\infty = 0.1$ [Fig. 8(e)], $\phi_\infty = 0.2$ [Fig. 8(f)] and $\phi_\infty = 1.0$ [Figs. 8(g)-(h)]. We note that, when increasing ϕ_∞ , dramatic changes arise. The regions not only change their sizes considerably, but they change the ways they are connected. The upper region for negative d becomes connected to the lower region with positive d when ϕ_∞ is increased from zero. Remarkably, the single branch of scalarized black holes splits into two branches with positive, resp. negative d . We see that the scalarized black holes for positive values of d have no limit of vanishing $\hat{\alpha}$ and, in fact, cease to exist if ϕ_∞ is as large as 0.2. Consequently, the wormhole solutions have no black-hole limit in this case. In this region, the domain of existence is limited by cusp-singularities only. Increasing ϕ_∞ further to the value $\phi_\infty = 1$, we note that the particle-like solutions with throat and equator (and wormholes) of the negative d region have moved to smaller values of $\hat{\alpha}$, whereas the ones of the positive d region are no longer visible in the figure. By increasing again the interval in $\hat{\alpha}$, as seen in Fig. 8(h), we see that this region has disappeared. Finally, we note that for quadratic coupling function and $\phi_\infty = 1$, the boundary of existence does not include the interval $0 < d < 0.1$ for $\hat{\alpha} \rightarrow 0$. Note that the domain of existence for negative values of ϕ_∞ can be obtained from the one with positive values of ϕ_∞ by reflection with respect to the $d = 0$ axis.

B. Cubic EsGB solutions

We now turn to the cubic coupling function $F = \alpha\phi^3$. Here, the domain of existence of particle-like solutions resides strictly in the negative d region (for positive coupling constant $\hat{\alpha}$). We exhibit their domain of existence (in blue colour) in Figs. 9(a)-(c), employing again the scaled scalar charge d and the scaled GB coupling constant $\hat{\alpha}$ to delimit its size.

In Fig. 9(a), we have chosen a vanishing boundary value for the scalar field at infinity, $\phi_\infty = 0$. We have also included the region of wormholes (in rose colour) which resides in the positive d region. As a result, there is no overlap between the particle-like solutions and the wormholes for the cubic coupling function. The boundaries of the domain of existence of particle-like solutions are again mainly determined by the occurrence of cusp singularities (denoted again by the dark blue line). In this case, Schwarzschild black holes (denoted by the dashed black line) are encountered for vanishing scalar charge d . The domain of existence of wormholes is also delimited by cusp singularities (blue line) and Schwarzschild black holes (black line), but also by scalarized black holes (denoted by the solid grey line). The latter solutions also reside strictly in the negative d region (for positive α).

As was illustrated in the case of the quadratic coupling, the domain of existence of particle-like solutions changes when the boundary value of the scalar field at infinity ϕ_∞ also changes. We demonstrate that this holds also for the cubic coupling function by choosing $\phi_\infty = 1$ in Fig. 9(b) and $\phi_\infty = -1$ in Fig. 9(c). From Fig. 9(b), we see that, when adopting a positive value for ϕ_∞ , the domain of existence gets restricted towards larger (absolute) values of d . For sufficiently negative ϕ_∞ , on the other hand, it seems that the domain is no longer bounded by cusp singularities but only by scalarized black holes. However, there is a tiny gap between the boundary of the particle-like solutions and the scalarized black hole solutions, not visible in Fig. 9(c).

C. Dilatonic EsGB solutions

We finally consider the domain of existence of particle-like solutions in the case of the dilatonic coupling function $F = \alpha e^{-\phi}$, in the plane again of the scale-invariant quantities $d = D/M$ and $\hat{\alpha} = 8\alpha/M^2$. We exhibit their domain of existence (in blue colour) in Fig. 9(d) for $\phi_\infty = 0$, restricting again to $\alpha \geq 0$. Now, particle-like

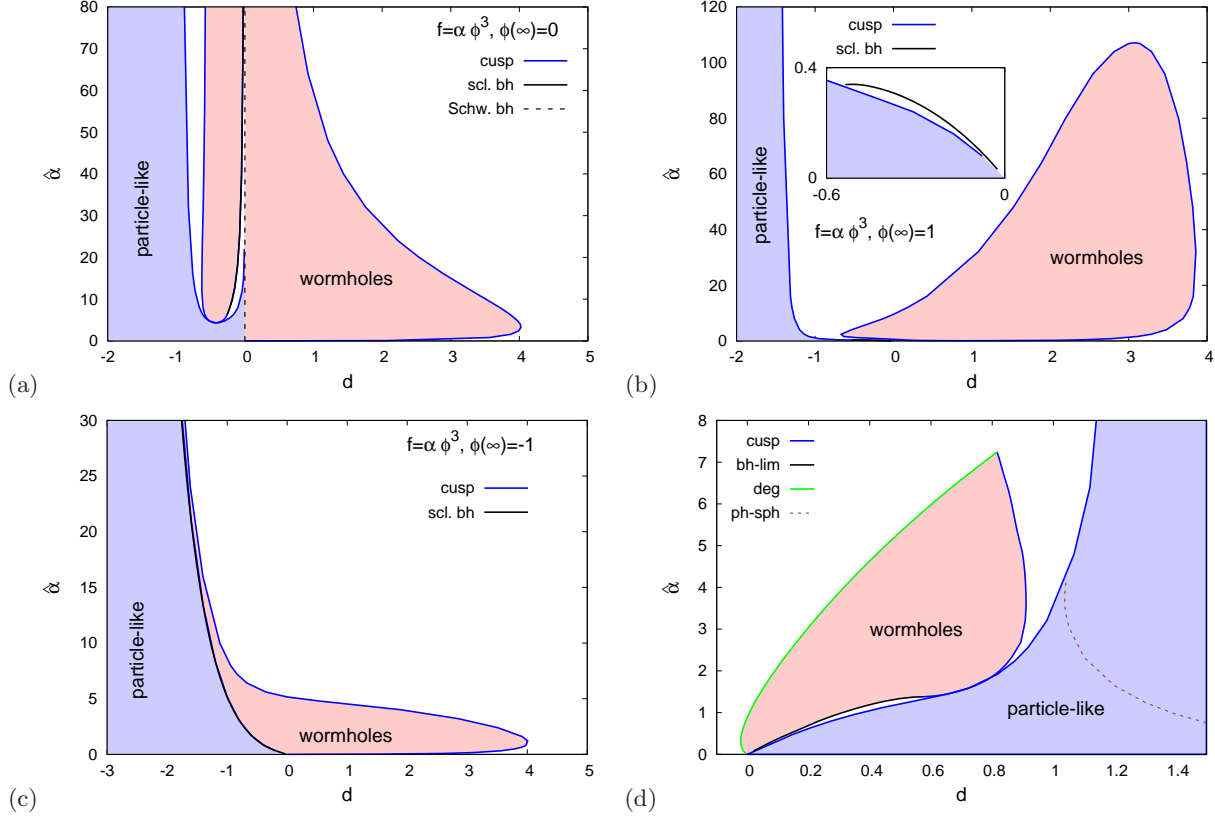


FIG. 9: (a)-(c) Domain of existence of particle-like solutions (in blue colour) in the $d - \hat{\alpha}$ plane for the cubic coupling function $F = \alpha \phi^3$ with $\phi_\infty = 0$ (a), $\phi_\infty = 1$ (b), and $\phi_\infty = -1$ (c); and for the dilatonic coupling function $F = \alpha e^{-\phi}$ with $\phi_\infty = 0$ (d). The boundaries of their domain of existence are given by cusp singularities (dark blue line) and black holes (solid grey line). The domain of wormholes is also indicated (in rose colour). The dashed red curve indicates the boundary of solutions for which lightrings exist. Solutions without lightrings are located above the dashed red curve.

solutions exist only in the positive d region. At the boundary of the domain, a cusp singularity (indicated by the blue line) is reached.

Also shown in Fig. 9(d) are the domain of existence of wormholes (again in rose colour) and the scalarized black holes (solid grey line), which form part of the boundary of the domain of existence of wormholes. Again, there is no overlap between the domains of existence of particle-like solutions and wormholes, although their boundaries lie quite close. For the dilatonic coupling function, all wormholes can be constructed from singular solutions.

VI. OBSERVATIONAL EFFECTS

We now discuss possible observational effects for these particle-like solutions. We first address their redshift. Then, we consider the effective stress-energy tensor to elucidate the high compactness of many of these solutions. Finally, we study the motion of both massive and massless particles in their gravitational background, and show that many particle-like solutions possess lightrings and can give rise to echoes in gravitational wave signals.

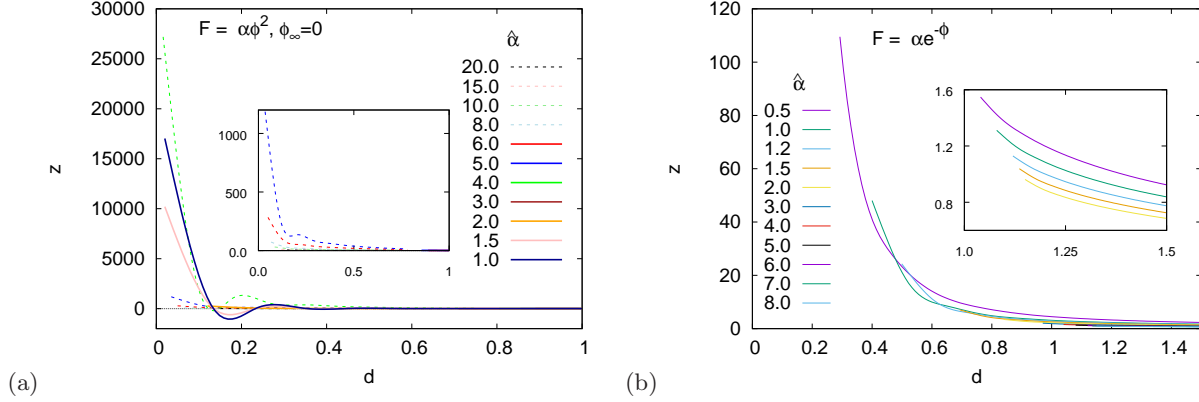


FIG. 10: The redshift z vs the dimensionless scalar charge d for the coupling functions $F = \alpha\phi^2$ (a) and $F = \alpha e^{-\phi}$ (b) with $\phi_\infty = 0$, and for several values of $\hat{\alpha}$.

A. Gravitational redshift

The redshift of a photon emitted by a source at the origin and seen by an observer in the asymptotic region is given by the redshift factor z , Eq. (29). It is therefore purely determined by the metric component $g_{tt}(0)$ at the origin. We exhibit a set of examples for the redshift factor z in Fig. 10, choosing the coupling function to be $F = \alpha\phi^2$ (a) and $F = \alpha e^{-\phi}$ (b) with $\phi_\infty = 0$, varying the scalar charge d and selecting several values of the GB coupling constant $\hat{\alpha}$.

Interestingly, as seen in Fig. 10(a) for particle-like solutions with quadratic coupling function and $\phi_\infty = 0$ the redshift factor can take both positive and negative values. The latter then correspond to a gravitational blueshift. For a quadratic coupling function with $\phi_\infty = 1$, we observe that the redshift factor increases with decreasing $\hat{\alpha}$, and takes very large values as the GR limit (Fisher solution) is approached. The analogous behavior is observed for a dilatonic coupling function.

B. Stress-energy tensor and compactness

Let us now consider the effective stress-energy tensor of the particle-like solutions. We exhibit the components T_t^t , T_r^r , and T_θ^θ in Figs. 11(a)-(d) again for the coupling functions $F = \alpha\phi^2$ with $\phi_\infty = 0$ and $F = \alpha e^{-\phi}$ for several values of $\hat{\alpha}$ and d . The figures show an interesting behavior of these components. Many particle-like solutions feature huge peaks in their energy density $\rho = -T_t^t$ and pressures T_r^r , and T_θ^θ . The energy density and the pressures are then strongly localized in a shell with a scaled circumferential radius R_c on the order of one. These particle-like solutions seem like (almost) empty bags, with the contributions from the scalar field and the GB term (almost) cancelling each other.

Figure 11 also shows the quantity $\mathcal{Q} = (-T_t^t + T_r^r)/N$ with $N = \sqrt{(T_t^t)^2 + (T_r^r)^2 + 2(T_\theta^\theta)^2}$. If $\mathcal{Q} < 0$ the null energy condition (NEC) is violated. We recall that the NEC is given by $T_{\mu\nu}n^\mu n^\nu \geq 0$, where n^μ is any null vector satisfying the condition $n^\mu n_\mu = 0$. Employing the null vector $n^\mu = (1, \sqrt{-g_{tt}/g_{rr}}, 0, 0)$ yields the condition $-T_t^t + T_r^r < 0$ for violation of the NEC to occur, while choosing $n^\mu = (1, 0, \sqrt{-g_{tt}/g_{\theta\theta}}, 0)$ leads to the condition $-T_t^t + T_\theta^\theta \geq 0$. Inspection of Figs. 11(g) and (h) shows that the presence of the GB term leads to violations of the NEC for the particle-like solutions, just as it does for wormholes [65]. The NEC is violated at small values of the scaled radial coordinate \hat{r} while it is restored as we move toward the asymptotic infinity.

We will now relate this very characteristic shell-like behavior of the particle-like solutions to their compactness. To that end, we define the mass function $\mu(\hat{R}_c)$, which is obtained by integrating the energy density $\rho = -T_t^t$

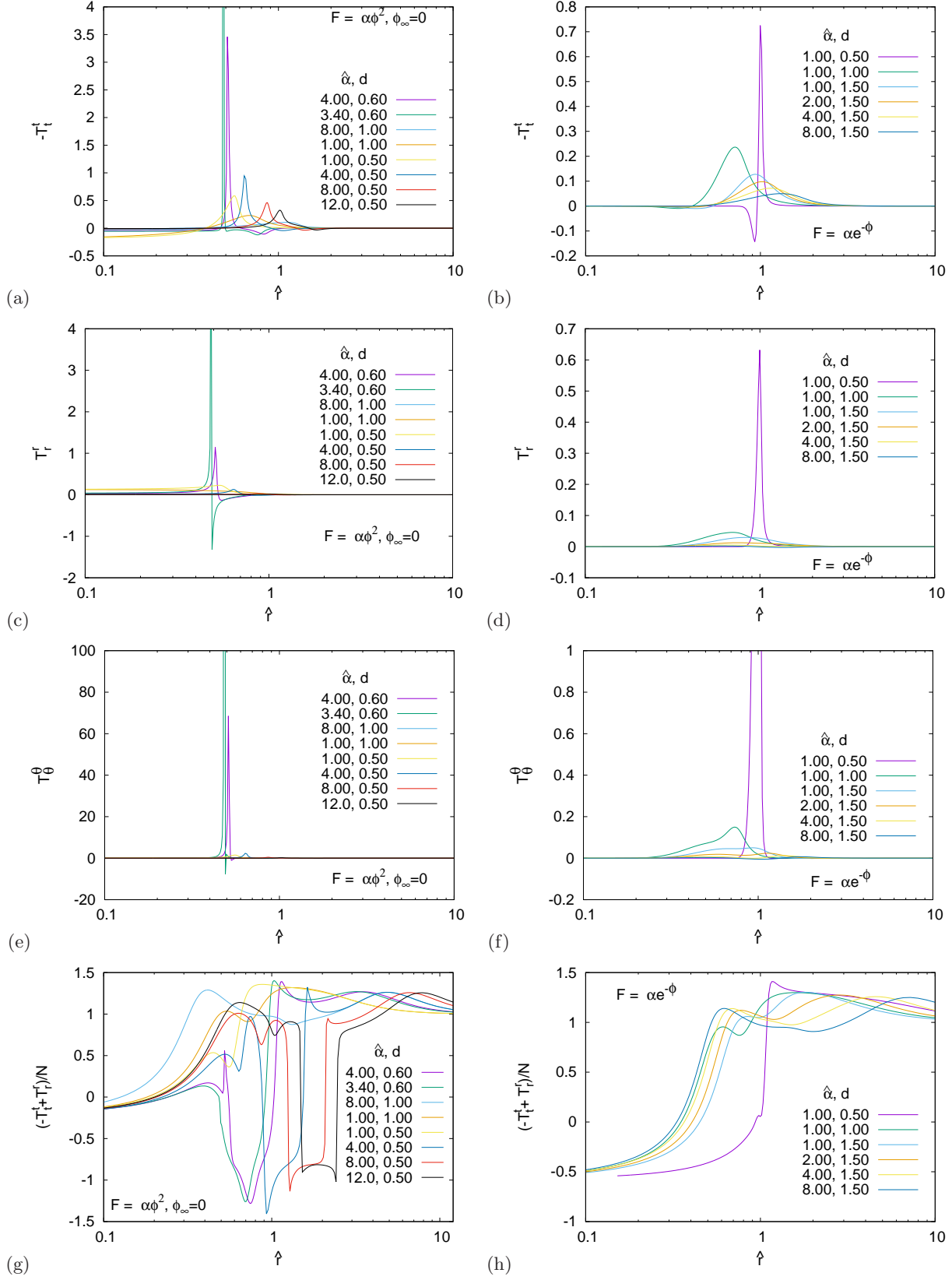


FIG. 11: (a)-(h) The components of the effective stress-energy tensor $-T_t^t$, T_r^r , and T_θ^θ and the quantity $(-T_t^t + T_r^r)/N$ with $N = \sqrt{(T_t^t)^2 + (T_r^r)^2 + 2(T_\theta^\theta)^2}$ vs the scaled radial coordinate \hat{r} for the coupling functions $F = \alpha\phi^2$ with $\phi_\infty = 0$ [left column: (a), (c), (e), (g)] and $F = \alpha e^{-\phi}$ [right column: (b), (d), (f), (h)], and several values of $\hat{\alpha}$ and d .

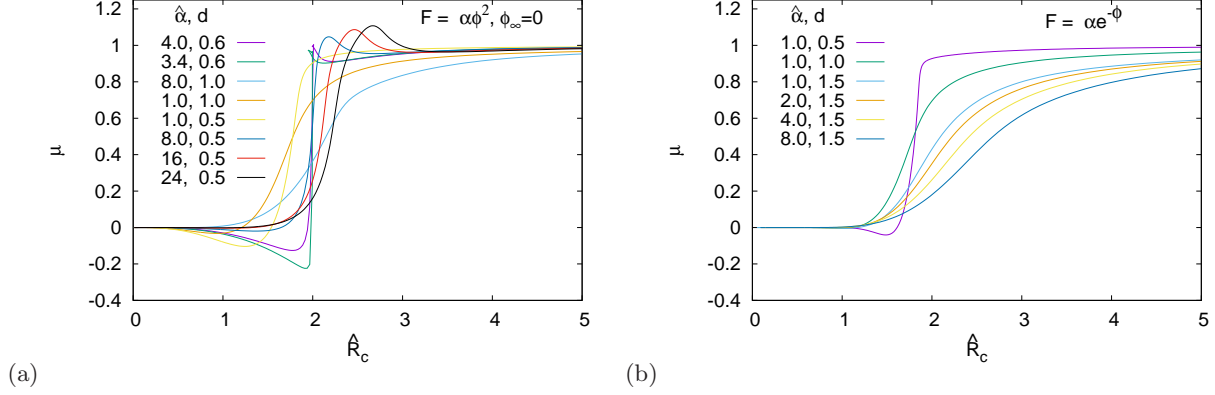


FIG. 12: The mass function $\mu(\hat{R}_c)$ vs the scaled circumferential radius \hat{R}_c for the coupling functions $F = \alpha\phi^2$ with $\phi_\infty = 0$ (a) and $F = \alpha e^{-\phi}$ (b), and several values of $\hat{\alpha}$ and d .

over a sphere with radius equal to the circumferential radius coordinate \hat{R}_c ,

$$\mu(\hat{R}_c) = -1/2 \int_0^{\hat{R}_c} T_t^t \hat{R}_c'^2 d\hat{R}_c' . \quad (44)$$

For these spherically symmetric solutions, the limit $\hat{R}_c \rightarrow \infty$ then yields precisely the mass of the solutions. The mass function $\mu(\hat{R}_c)$ is illustrated in Fig. 12 for the coupling functions $F = \alpha\phi^2$ with $\phi_\infty = 0$ (a) and $F = \alpha e^{-\phi}$ (b), and for several values of $\hat{\alpha}$ and d .

Figure 12 shows that the mass function $\mu(\hat{R}_c)$ exhibits a characteristic steep rise towards its asymptotic value in the vicinity of $\hat{R}_c = 2$ for many of the particle-like solutions. Here such a rise is, in fact, expected from the shell-like behaviour of the energy density, as seen in Fig. 11. The mass of the solutions then resides to a large extent in a very small region, qualifying these particle-like solutions as highly compact objects. Let us recall that for Schwarzschild black holes $\hat{R}_c = 2$ corresponds precisely to the scaled horizon radius. This characteristic behavior holds for both the quadratic and the dilatonic coupling functions. We will next show that these highly compact solutions will then also feature lightrings.

C. Lightrings

In order to obtain the lightrings formed around our particle-like solutions, we need to consider the geodesics of light in these static, spherically-symmetric spacetimes. We may obtain the geodesics for both null and timelike particles from their Lagrangian \mathcal{L} given by the expression

$$2\mathcal{L} = g_{\mu\nu} \dot{x}^\mu \dot{x}^\nu = -e^{f_0} \dot{t}^2 + e^{f_1} \left[\dot{r}^2 + r^2 \left(\dot{\theta}^2 + \sin^2 \theta \dot{\varphi}^2 \right) \right] = -\epsilon , \quad (45)$$

where $\epsilon = 0$ and 1 for massless and massive particles, respectively. Here, we assume that these test particles possess no direct coupling to the scalar field. The independence of \mathcal{L} of the coordinates t and φ leads to two conserved quantities, namely the energy E and the angular-momentum L of the particle

$$E = -e^{f_0} \dot{t} , \quad (46)$$

$$L = e^{f_1} r^2 \dot{\varphi} . \quad (47)$$

Inserting these expressions into the Lagrangian and considering motion in the equatorial plane ($\theta = \pi/2$), we obtain for the radial coordinate the equation

$$e^{f_0+f_1} \dot{r}^2 = E^2 - \epsilon e^{f_0} - \frac{e^{f_0-f_1} L^2}{r^2} . \quad (48)$$

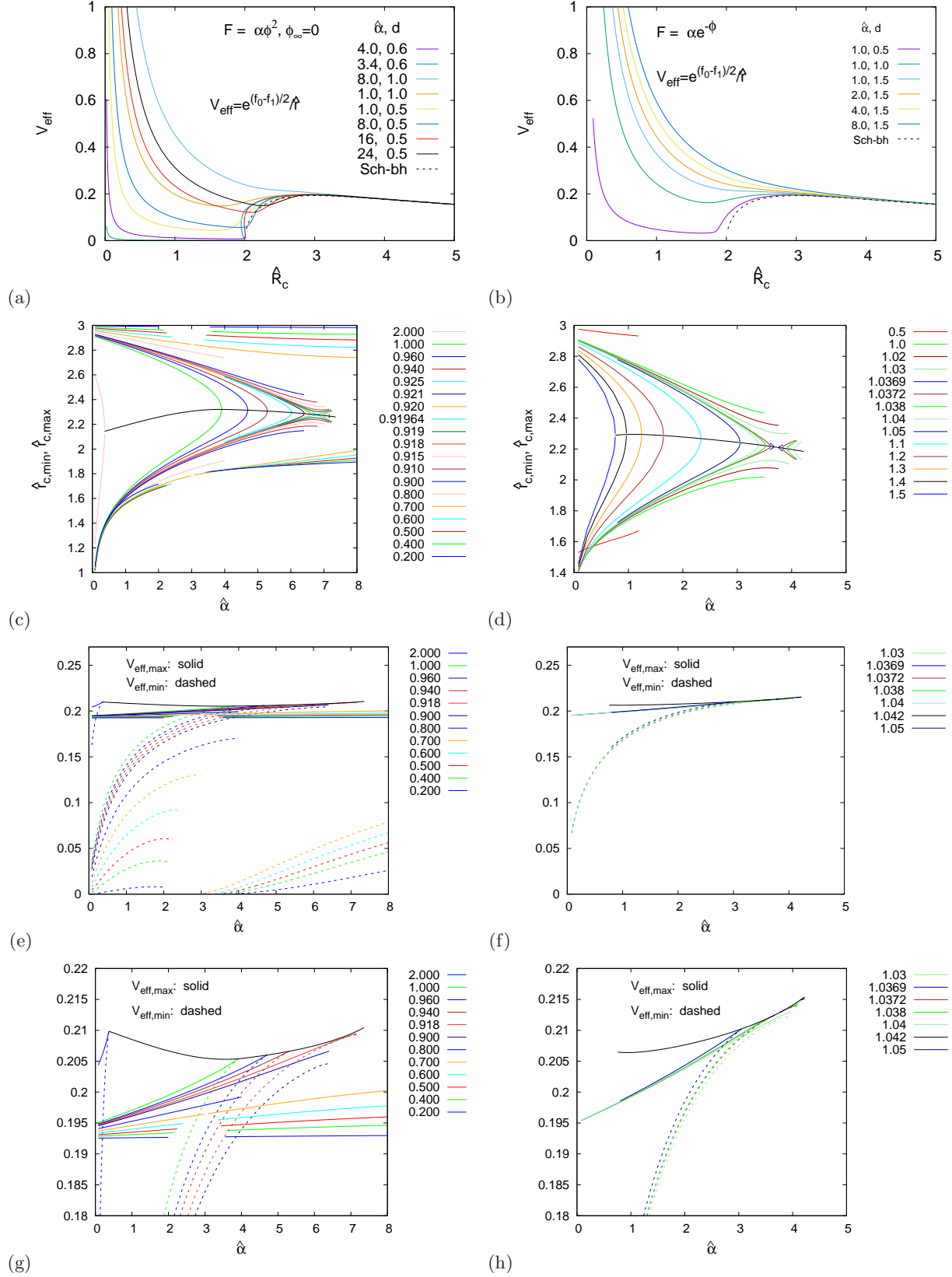


FIG. 13: (a)-(b) The photon effective potential V_{eff} vs the scaled circumferential coordinate \hat{R}_c , for several values of $\hat{\alpha}$ and d ; (c)-(d) the locations of the local maxima $\hat{R}_{c,\text{max}}$ and minima $\hat{R}_{c,\text{min}}$ vs $\hat{\alpha}$, for several values of d ; (e)-(f) the local maxima (solid lines) and minima (dashed lines) of the effective potential vs $\hat{\alpha}$, for several values of d ; (g)-(h) a zoom of (e)-(f). The coupling functions are $F = \alpha\phi^2$ with $\phi_\infty = 0$ [left column: (a), (c), (e), (g)] and $F = \alpha e^{-\phi}$ [right column: (b), (d), (f), (h)].

Let us first consider the radial equation for photons ($\epsilon = 0$). In this case, we find

$$e^{f_0+f_1}\dot{r}^2 = (E + LV_{\text{eff}})(E - LV_{\text{eff}}), \quad (49)$$

where V_{eff} is the effective potential for photons

$$V_{\text{eff}} = e^{(f_0-f_1)/2}/r. \quad (50)$$

The effective potential V_{eff} vs the scaled circumferential coordinate \hat{R}_c is shown in Fig. 13, for several values of $\hat{\alpha}$ and d , and employing the coupling functions $F = \alpha\phi^2$ with $\phi_\infty = 0$ (a) and $F = \alpha e^{-\phi}$ (b). For the less compact particle-like solutions, the effective potential is monotonic. As the energy density gets more localized, the effective potential V_{eff} develops a saddle point, which splits into a pair of extrema upon further change of the parameters, leading to a still stronger localization of the energy density and an increasing compactness of the solutions.

Lightrings correspond to extrema of the effective potential V_{eff} , since they correspond to photon geodesics with fixed radial coordinate. Our analysis shows, that the particle-like solutions either possess no lightring at all, or they possess a pair of lightrings, consisting of a local maximum $\hat{R}_{c,\text{max}}$ at larger r and a local minimum $\hat{R}_{c,\text{min}}$ at smaller r . In Figs. 13(c) and (d), the locations of the local maxima $\hat{R}_{c,\text{max}}$ and minima $\hat{R}_{c,\text{min}}$ are shown versus $\hat{\alpha}$, for several values of d and the coupling functions $F = \alpha\phi^2$ with $\phi_\infty = 0$ (c) and $F = \alpha e^{-\phi}$ (d). Also indicated are the saddle points, where $\hat{R}_{c,\text{max}}$ and $\hat{R}_{c,\text{min}}$ emerge. In the figures showing the domains of existence, Figs. 8 and Figs. 9, we have marked, by using dashed curves, where particle-like solutions with lightrings emerge.

The local maxima and minima of the effective potential V_{eff} are exhibited in Figs. 13(e) and (f) (with Figs. 13(g) and (h) representing amplifications). Clearly, photons with energies smaller than the value of $L V_{\text{eff}}$ at its local maximum, that reside inside the potential well, remain in bound orbits in the spacetimes of the particle-like solutions. Therefore, the lightrings at the minima of the potentials represent stable photon orbits. In contrast, the maxima represent unstable bound photon orbits. We emphasize that the presence of lightrings qualifies the respective particle-like solutions as UCOs [71].

The fact that lightrings can only be present in pairs in the spacetime of our particle-like solutions is in accordance with a theorem on lightrings of UCOs [74]. There, it is also shown that, in a smooth spherically-symmetric metric, one of the lightrings should be stable, which also agrees with our findings for the particle-like solutions. Let us finally mention that it has recently been pointed out that the presence of a stable lightring might lead to nonlinear spacetime instabilities [85, 86]. So far the arguments involved are in a preliminary stage, and will need further investigation.

D. Particle motion

For massive test particles, we introduce the effective potential V_{eff}^m by starting again from the radial equation (48) and setting $\epsilon = 1$. In that case, we obtain

$$e^{f_0+f_1}\dot{r}^2 = (E + V_{\text{eff}}^m)(E - V_{\text{eff}}^m). \quad (51)$$

Then, V_{eff}^m is given by

$$V_{\text{eff}}^m = \sqrt{e^{f_0} + \frac{e^{f_0-f_1}L^2}{r^2}}. \quad (52)$$

The effective potential V_{eff}^m is shown in Figs. 14(a) and (b) as a function of the scaled circumferential coordinate \hat{R}_c , choosing the coupling functions $F = \alpha\phi^2$ with $\phi_\infty = 0$ (a) and $F = \alpha e^{-\phi}$ (b) and the parameters $\hat{\alpha} = 1$ and $d = 1$, corresponding to highly compact particle-like solutions.

In these figures, the particle angular momentum L is varied, to illustrate the interesting features of the angular momentum barrier for these solutions. The dashed curves correspond to particle motion in the spacetime of a Schwarzschild black hole with the same mass ($M = 1$). The vertical line corresponds to the event horizon. We note that the effective potential V_{eff}^m follows very closely the effective potential in the Schwarzschild spacetime

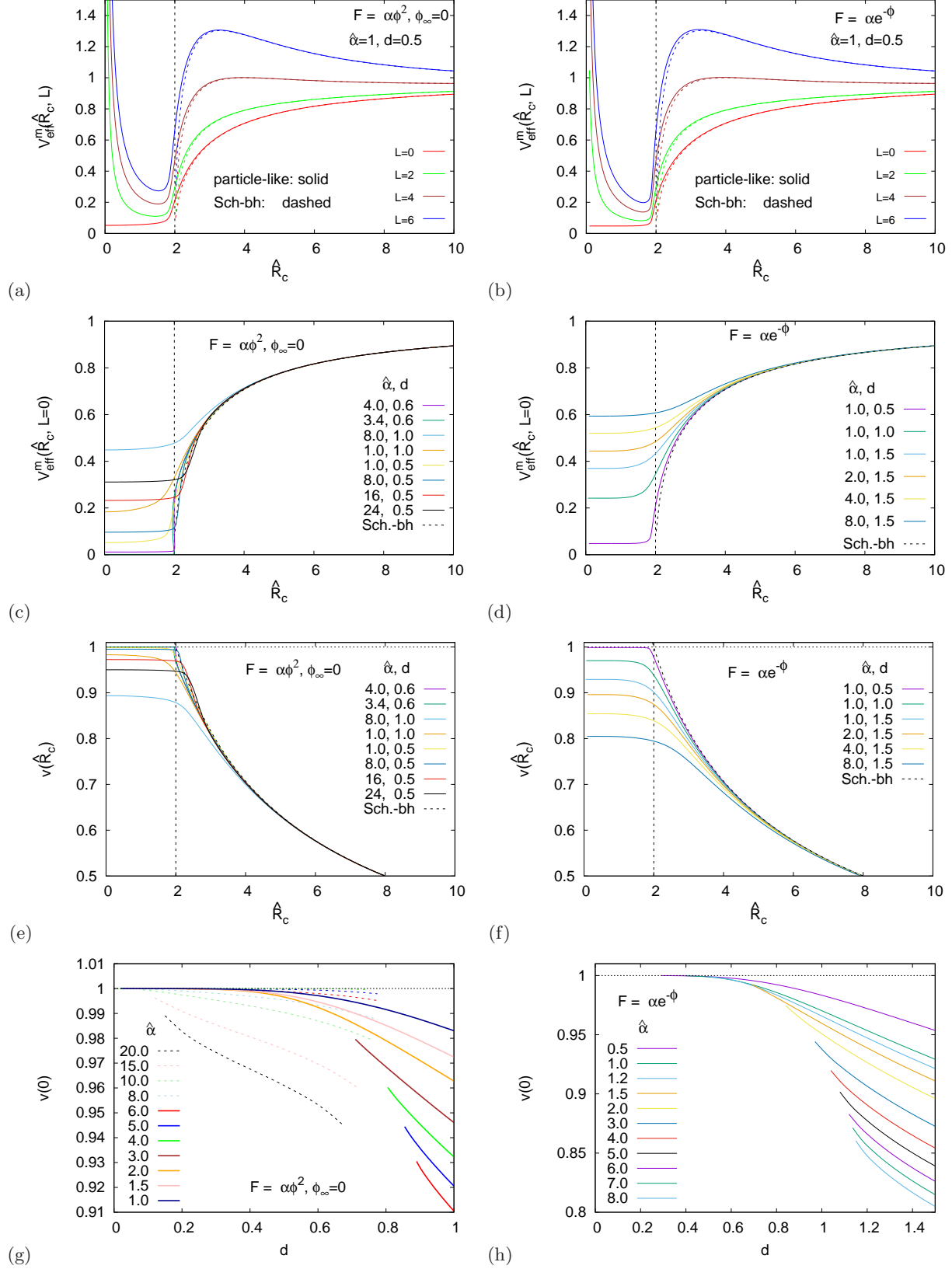


FIG. 14: (a)-(b) The effective potential V_{eff}^m for massive particles vs the scaled circumferential coordinate \hat{R}_c , for several values of the angular momentum L and for $\hat{\alpha} = 1$, $d = 1$ (Schwarzschild: dashed lines, event horizon: vertical line); (c)-(d) V_{eff}^m for radial motion ($L = 0$) in several spacetimes; (e)-(f) the speed v of radially infalling test particles ($L = 0$); (g)-(h) the maximal speed $v_{\text{max}} = v(0)$ of radially infalling test particles ($L = 0$). The coupling functions are $F = \alpha\phi^2$ with $\phi_\infty = 0$ [left column: (a), (c), (e), (g)] and $F = \alpha e^{-\phi}$ [right column: (b), (d), (f), (h)].

in most of the outer region. Only close to the black hole horizon, which resides at the scaled circumferential radius $\hat{R}_c = 2$, the respective effective potentials for the massive test particle in the black-hole and particle-like spacetimes start to deviate. Inside $\hat{R}_c = 2$, the effective potential V_{eff}^m of the particle-like solutions then exhibits a completely different behavior. Instead of turning negative, the effective potential V_{eff}^m remains always positive. In fact, it reaches a minimum, and then diverges at the origin when L is non-zero. Thus, while the motion of particles beyond $\hat{R}_c = 2$ will be very similar to the motion in a black-hole spacetime, the absence of an event horizon and the regularity of the spacetime at the center allow for a very different type of motion in the inner region. In particular, there are always bound orbits of massive particles, although these may be confined to reside close to the center of the spacetime.

To see that the divergence of the scalar field at the origin does not affect the motion in the spacetime, and that a particle may reach and pass over the origin without encountering any influence of this divergence, we now set the angular momentum of the particle to zero. The effective potential V_{eff}^m for radial motion ($L = 0$) in a variety of spacetimes is illustrated in Figs. 14(c) and (d). We see that the effective potential is always regular at the center, where it also assumes its minimal value. Thus, a particle could sit at rest right at the center. Also bound oscillating motion across the center is possible, as observed also in other regular spacetimes [87]. In Figs. 14(e) and (f), we illustrate, for the same set of spacetimes, the speed v of radially infalling test particles ($L = 0$), which all possess a speed of half the velocity of light ($v = 0.5$) at a circumferential radius $\hat{R}_c = 8$. Again, comparison with the Schwarzschild black hole is made in the figures. Figures 14(g) and (h) finally show the maximal speed $v_{\text{max}} = v(0)$ of radially infalling test particles ($L = 0$) as a function of the scaled scalar charge d , for several values of $\hat{\alpha}$.

E. Echoes of UCOs

Lastly, we will address possible signatures of the ultra-compact particle-like solutions in the framework of gravitational-wave spectroscopy. As pointed out in [69–71], because of the absence of an event horizon, UCOs might reveal themselves in the ringdown phase of a merger event, since they will give rise to secondary pulses in the ringdown waveform, i.e., to a sequence of echoes.

To demonstrate the occurrence of echoes for the ultra-compact particle-like solutions, we consider a simple scattering process of a test scalar wave Ψ by the gravitational potential of the UCO. In particular, we expand the scalar wave in spherical harmonics $Y_l^m(\theta, \varphi)$,

$$\Psi(t, r, \theta, \varphi) = \sum_{l,m} \psi_{l,m}(t, r) e^{-f_1/2} Y_l^m(\theta, \varphi) / r, \quad (53)$$

and insert this expansion into the free Klein-Gordon equation,

$$\partial_\mu(\sqrt{-g} \partial^\mu \Psi) = 0. \quad (54)$$

This then results in the following equation for $\psi_{l,m}(t, r)$

$$(\partial_t^2 - \partial_{r_*}^2 + V_{\text{eff}}^\psi) \psi_{l,m}(t, r) = 0. \quad (55)$$

Here, we have introduced the tortoise coordinate r_* defined as

$$r_* = \int_0^r e^{(f_1 - f_0)/2} dr, \quad (56)$$

where the integration constant is chosen such that $r_* = 0$ corresponds to the origin. We have also defined the l -dependent effective potential V_{eff}^ψ ,

$$V_{\text{eff}}^\psi = e^{f_0 - f_1} \left[\frac{l(l+1)}{r^2} + \frac{2(f'_1 + f'_0) + r f'_1 f'_0 + 2r f''_1}{4r} \right]. \quad (57)$$

Let us now inspect the profile of V_{eff}^ψ . We exhibit the scaled effective potential $M^2 V_{\text{eff}}^\psi$ versus the scaled tortoise coordinate r_*/M in Figs. 15 for a set of particle-like solutions with coupling functions $F = \alpha \phi^2$ with

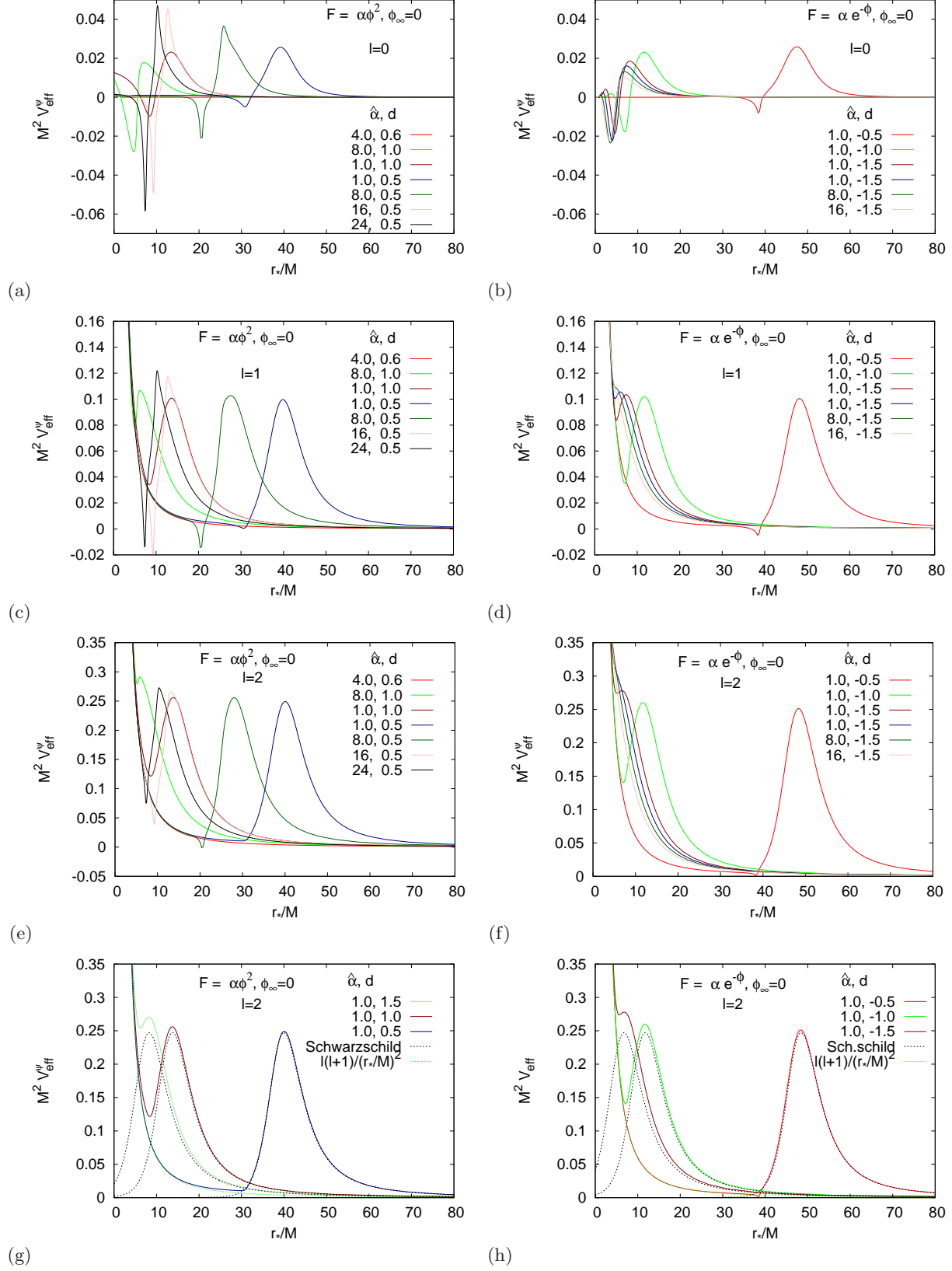


FIG. 15: (a)-(h) The scaled effective potential $M^2 V_{\text{eff}}^{\psi}$ vs the scaled tortoise coordinate r_*/M for a test scalar particle with angular momentum numbers $l = 0$ (a)-(b), $l = 1$ (c)-(d), and $l = 2$ (e)-(h) for a set of particle-like solutions with coupling functions $F = \alpha \phi^2$ with $\phi_{\infty} = 0$ [left column: (a), (c), (e), (g)] and $F = \alpha e^{-\phi}$ [right column: (b), (d), (f), (h)]. In (g) and (h), also the effective potential in the Schwarzschild black-hole spacetime is shown (black dashed line).

$\phi_\infty = 0$ [left column: (a), (c), (e), (g)] and $F = \alpha e^{-\phi}$ [right column: (b), (d), (f), (h)]. For the test scalar wave, we have chosen the angular momentum numbers $l = 0$ [Figs. 15(a)-(b)], $l = 1$ [Figs. 15(c)-(d)], and $l = 2$ [Figs. 15(e)-(h)]. From Figs. 15(a)-(b), we observe that, for a scalar wave with $l = 0$, the effective potential V_{eff}^ψ acquires a finite value near the origin and for both coupling functions. However, V_{eff}^ψ diverges at the origin $r = 0$, when $l > 0$, as seen in Figs. 15(c)-(h). Thus, also for a test scalar wave with $l > 0$ an infinite angular momentum barrier resides at the origin. In addition, there is the usual finite local barrier, located at a larger value of r_* , that is also present for black holes.

We now consider an incoming test scalar-wave with modes with $l > 0$. These modes will then be partially transmitted through the finite local barrier and partially reflected back to infinity. The transmitted modes will then be fully reflected by the infinite angular momentum barrier. Upon reaching the local barrier, the reflected modes will be partially transmitted through the finite local barrier and partially reflected again. Thus, we observe a perpetual process of full and partial reflection between the angular-momentum and the local barrier, respectively. As a result, we will see an infinite number of echoes, which possess an amplitude that is decreasing every time that the wave gets partially transmitted through the local barrier, as it moves outwards.

In Figs. 15(g) and (h) we compare the effective potential V_{eff}^ψ in several UCO spacetimes with the effective potential in the Schwarzschild spacetime (dashed black line). Here the integration constant for the tortoise coordinate for the Schwarzschild solution is chosen such that the local maxima for V_{eff}^ψ in the particle-like and Schwarzschild spacetimes coincide. Again, we note that in the outer region the effective potentials agree very well, whereas in the inner region the behavior is very different, since the black hole effective potential features only the finite local barrier, and any modes passing this barrier will disappear behind the horizon. So only a single reflection will be seen for a wave impinging on a black hole. The observation of the presence of echoes in a wave signal will thus reveal the lack of a horizon of the compact object.

VII. CONCLUSIONS

We have investigated a new type of solutions of EsGB theories, employing a variety of coupling functions for the scalar field [73]. These particle-like solutions are asymptotically flat, and possess a globally regular metric. While the scalar field diverges as $1/r$ at the origin, this divergence is cancelled in the effective stress-energy tensor by contributions from the GB term, yielding a regular effective stress-energy tensor and thus a regular source term in the Einstein equations. When taking the GB coupling constant to zero, on the other hand, the singular Fisher (JNWW) solution of GR is recovered. Let us add, that regular particle-like solutions have also been found in Einstein-scalar Maxwell theories with various coupling functions [88].

We have presented the domain of existence of these particle-like solutions in detail for quadratic, cubic and dilaton coupling functions, allowing for either a vanishing or finite (cosmological) values of the scalar field at asymptotic infinity, ϕ_∞ . For quadratic coupling and vanishing ϕ_∞ , the solutions are symmetric with respect to $\phi \rightarrow -\phi$, and thus the domain of existence is symmetric with respect to positive and negative scalar charge. The symmetry is broken when $\phi_\infty \neq 0$, or when a non-symmetric coupling is employed.

In the case of a quadratic coupling and $\phi_\infty = 0$, the domain of existence of particle-like solutions has an overlap with the domain of wormhole solutions. The reason is the occurrence of particle-like solutions which feature a throat and an equator. In this case, wormhole solutions can be constructed by continuing symmetrically at the throat or equator (after a suitable coordinate transformation) with a second asymptotically flat spacetime [65]. The domain of existence of particle-like solutions consists of a tower of distinct regions, that differ in the number of nodes of the scalar-field function. We note that both the tower of distinct regions and the overlap between particle-like and wormhole solutions are characteristic features of the domain of existence for the quadratic coupling function - the respective domains for the cubic or dilatonic coupling functions feature no distinct regions, as the coupling constant increases, and no overlap is found between the domains of the particle-like and wormhole solutions (which are again present in the solution space of the theory as shown in [65].)

The boundary of the domain of existence of the particle-like solutions is formed by solutions with singularities. Mostly a cusp singularity is encountered at the boundary, but also an ordinary curvature singularity can be encountered. Only in the case of the cubic coupling with negative ϕ_∞ , we have encountered a boundary formed by scalarized black holes.

However, the focus of the paper has been the study of the properties of these particle-like solutions. Here we have first investigated the redshift function z of these solutions, which can assume very large values. Interestingly, for the quadratic coupling function with $\phi_\infty = 0$ also negative values of z are found corresponding to blueshift.

Next, we have addressed the compactness of these particle-like solutions. By investigating the effective stress-energy tensor, we have seen that the energy density and pressure can be highly localized. This yields a shell-like structure of the solutions corresponding to almost empty bags in terms of the energy density. For these solutions, the mass function rises very steeply in the vicinity of the circumferential radius $R_c = 2M$, which would correspond to the horizon of a Schwarzschild black hole. In this case, then, the solutions are highly compact.

Subsequently, we have considered the geodesics in these spacetimes. To show that many of the solutions qualify as UCOs, we have investigated the presence of lightrings. As predicted on general grounds [74], the lightrings of these particle-like solutions always come in pairs. The outer unstable lightring corresponds to the lightring of the Schwarzschild spacetime. But an inner stable lightring occurs as well, due to the diverging (at the origin) angular momentum barrier of these regular spacetimes. Thus, there are stable bound photon orbits in these spacetimes.

Ordinary massive particles moving in these spacetimes do not feel the divergence of the scalar field at the origin. They simply see the gravitational field as given by the regular spacetime metric. Thus these particles can pass over the center of the spacetime unhindered, they can oscillate across the center or even remain stationary at the center. If they carry angular momentum, the presence of the infinite angular momentum barrier at the center will always allow for bound particle motion.

Lastly, we have addressed possible gravitational-wave signals for these ultra-compact spacetimes, showing the presence of echoes in the asymptotic wave signal. This was to be expected on general grounds because of the absence of horizons in these particle-like solutions [69–71]. In particular, we have studied the effective potential for a scalar wave, which again features two barriers, a finite local barrier and an infinite angular momentum barrier at the center. An incoming wave will thus be fully reflected every time it encounters the infinite central barrier, but only partly reflected, every time it encounters the finite outer barrier. This sequence of reflections will then give rise to a sequence of echoes with decreasing amplitude in the gravitational wave signal, not present in signals from black holes.

Open questions to be answered in future work concern the stability of these solutions. In particular, a quasi-normal mode analysis could be performed, as has already been (partly) performed for EsGB black holes and wormholes. It would also be interesting to address the existence of rotating generalizations of these particle-like solutions and of the associated wormholes. So far only rotating EsGB black holes and their properties, including their shadow, have been studied.

VIII. ACKNOWLEDGMENTS

BK and JK gratefully acknowledge support by the DFG Research Training Group 1620 *Models of Gravity* and the COST Actions CA15117 and CA16104. BK and PK acknowledge helpful discussions with Eugen Radu and Athanasios Bakopoulos, respectively.

-
- [1] C. M. Will, *Living Rev. Rel.* **9**, 3 (2006)
 - [2] V. Faraoni and S. Capozziello, *Fundam. Theor. Phys.* **170** (2010)
 - [3] E. Berti *et al.*, *Class. Quant. Grav.* **32**, 243001 (2015)
 - [4] T. P. Sotiriou, *Lect. Notes Phys.* **892**, 3 (2015)
 - [5] G. W. Horndeski, *Int. J. Theor. Phys.* **10**, 363 (1974).
 - [6] C. Charmousis, E. J. Copeland, A. Padilla and P. M. Saffin, *Phys. Rev. Lett.* **108**, 051101 (2012)
 - [7] T. Kobayashi, M. Yamaguchi and J. Yokoyama, *Prog. Theor. Phys.* **126**, 511 (2011)
 - [8] B. Zwiebach, *Phys. Lett.* **156B**, 315 (1985).
 - [9] D. J. Gross and J. H. Sloan, *Nucl. Phys. B* **291**, 41 (1987).
 - [10] R. R. Metsaev, A. A. Tseytlin, *Nucl. Phys.* **B293**, 385 (1987).
 - [11] P. Kanti, N. E. Mavromatos, J. Rizos, K. Tamvakis and E. Winstanley, *Phys. Rev. D* **54** (1996) 5049.

- [12] T. Torii, H. Yajima and K. i. Maeda, Phys. Rev. D **55**, 739 (1997)
- [13] Z. K. Guo, N. Ohta and T. Torii, Prog. Theor. Phys. **120**, 581 (2008)
- [14] P. Pani and V. Cardoso, Phys. Rev. D **79**, 084031 (2009)
- [15] P. Pani, C. F. B. Macedo, L. C. B. Crispino and V. Cardoso, Phys. Rev. D **84**, 087501 (2011)
- [16] B. Kleihaus, J. Kunz and E. Radu, Phys. Rev. Lett. **106** (2011) 151104.
- [17] D. Ayzenberg, K. Yagi and N. Yunes, Phys. Rev. D **89**, no. 4, 044023 (2014)
- [18] D. Ayzenberg and N. Yunes, Phys. Rev. D **90**, 044066 (2014)
- [19] A. Maselli, P. Pani, L. Gualtieri and V. Ferrari, Phys. Rev. D **92**, no. 8, 083014 (2015)
- [20] B. Kleihaus, J. Kunz and S. Mojica, Phys. Rev. D **90**, no. 6, 061501 (2014)
- [21] B. Kleihaus, J. Kunz, S. Mojica and E. Radu, Phys. Rev. D **93**, no. 4, 044047 (2016)
- [22] J. L. Blázquez-Salcedo, C. F. B. Macedo, V. Cardoso, V. Ferrari, L. Gualtieri, F. S. Khoo, J. Kunz and P. Pani, Phys. Rev. D **94**, no. 10, 104024 (2016)
- [23] P. V. P. Cunha, C. A. R. Herdeiro, B. Kleihaus, J. Kunz and E. Radu, Phys. Lett. B **768**, 373 (2017)
- [24] H. Zhang, M. Zhou, C. Bambi, B. Kleihaus, J. Kunz and E. Radu, Phys. Rev. D **95**, no. 10, 104043 (2017)
- [25] J. L. Blázquez-Salcedo, F. S. Khoo and J. Kunz, Phys. Rev. D **96**, no.6, 064008 (2017)
- [26] R. Konoplya, A. Zinhailo and Z. Stuchlik, Phys. Rev. D **99**, no.12, 124042 (2019)
- [27] A. Zinhailo, Eur. Phys. J. C **79**, no.11, 912 (2019)
- [28] P. T. Chrusciel, J. Lopes Costa and M. Heusler, Living Rev. Rel. **15**, 7 (2012) [arXiv:1205.6112 [gr-qc]].
- [29] C. A. R. Herdeiro and E. Radu, Int. J. Mod. Phys. D **24**, no. 09, 1542014 (2015) [arXiv:1504.08209 [gr-qc]].
- [30] P. Kanti, B. Kleihaus and J. Kunz, Phys. Rev. Lett. **107** (2011) 271101.
- [31] P. Kanti, B. Kleihaus and J. Kunz, Phys. Rev. D **85** (2012) 044007.
- [32] M. A. Cuyubamba, R. A. Konoplya and A. Zhidenko, Phys. Rev. D **98**, no. 4, 044040 (2018).
- [33] H. G. Ellis, J. Math. Phys. **14**, 104 (1973).
- [34] H. G. Ellis, Gen. Rel. Grav. **10**, 105 (1979).
- [35] K. A. Bronnikov, Acta Phys. Polon. B **4**, 251 (1973).
- [36] T. Kodama, Phys. Rev. D **18**, 3529 (1978).
- [37] M. S. Morris and K. S. Thorne, Am. J. Phys. **56** (1988) 395.
- [38] M. Visser, “Lorentzian wormholes: From Einstein to Hawking,” Woodbury, USA: AIP (1995)
- [39] B. Kleihaus and J. Kunz, Phys. Rev. D **90**, 121503 (2014)
- [40] X. Y. Chew, B. Kleihaus and J. Kunz, Phys. Rev. D **94**, no. 10, 104031 (2016)
- [41] G. Antoniou, A. Bakopoulos and P. Kanti, Phys. Rev. Lett. **120**, no. 13, 131102 (2018);
- [42] D. D. Doneva and S. S. Yazadjiev, Phys. Rev. Lett. **120**, no. 13, 131103 (2018).
- [43] H. O. Silva, J. Sakstein, L. Gualtieri, T. P. Sotiriou and E. Berti, Phys. Rev. Lett. **120**, no. 13, 131104 (2018).
- [44] G. Antoniou, A. Bakopoulos and P. Kanti, Phys. Rev. D **97**, no. 8, 084037 (2018)
- [45] J. L. Blázquez-Salcedo, D. D. Doneva, J. Kunz and S. S. Yazadjiev, Phys. Rev. D **98**, no. 8, 084011 (2018).
- [46] D. D. Doneva, S. Kiorpelidi, P. G. Nedkova, E. Papantonopoulos and S. S. Yazadjiev, Phys. Rev. D **98**, no.10, 104056 (2018)
- [47] M. Minamitsuji and T. Ikeda, Phys. Rev. D **99**, no. 4, 044017 (2019)
- [48] H. O. Silva, C. F. B. Macedo, T. P. Sotiriou, L. Gualtieri, J. Sakstein and E. Berti, Phys. Rev. D **99**, no. 6, 064011 (2019)
- [49] Y. Brihaye and L. Ducobu, Phys. Lett. B **795**, 135 (2019)
- [50] Y. S. Myung and D. Zou, Phys. Lett. B **790**, 400-407 (2019)
- [51] A. Bakopoulos, G. Antoniou and P. Kanti, Phys. Rev. D **99**, no.6, 064003 (2019)
- [52] D. D. Doneva, K. V. Staykov and S. S. Yazadjiev, Phys. Rev. D **99**, no. 10, 104045 (2019)
- [53] Y. S. Myung and D. C. Zou, Int. J. Mod. Phys. D **28**, no. 09, 1950114 (2019)
- [54] C. F. B. Macedo, J. Sakstein, E. Berti, L. Gualtieri, H. O. Silva and T. P. Sotiriou, Phys. Rev. D **99**, no. 10, 104041 (2019)
- [55] P. V. P. Cunha, C. A. R. Herdeiro and E. Radu, Phys. Rev. Lett. **123**, no. 1, 011101 (2019)
- [56] A. Bakopoulos, P. Kanti and N. Pappas, Phys. Rev. D **101**, no.4, 044026 (2020)
- [57] S. Hod, Phys. Rev. D **100** (2019) no.6, 064039
- [58] L. G. Collodel, B. Kleihaus, J. Kunz and E. Berti, Class. Quant. Grav. **37**, no.7, 075018 (2020)
- [59] A. Bakopoulos, P. Kanti and N. Pappas, Phys. Rev. D **101**, no.8, 084059 (2020)
- [60] J. L. Blázquez-Salcedo, D. D. Doneva, S. Kahlen, J. Kunz, P. Nedkova and S. S. Yazadjiev, Phys. Rev. D **101** (2020) no.10, 104006
- [61] T. Damour and G. Esposito-Farese, Phys. Rev. Lett. **70**, 2220-2223 (1993)
- [62] T. P. Sotiriou and S. Y. Zhou, Phys. Rev. Lett. **112**, 251102 (2014)
- [63] T. P. Sotiriou and S. Y. Zhou, Phys. Rev. D **90**, 124063 (2014)
- [64] J. F. Delgado, C. A. Herdeiro and E. Radu, [arXiv:2002.05012 [gr-qc]].
- [65] G. Antoniou, A. Bakopoulos, P. Kanti, B. Kleihaus and J. Kunz, Phys. Rev. D **101**, no.2, 024033 (2020)

- [66] V. Cardoso and L. Gualtieri, *Class. Quant. Grav.* **33**, no. 17, 174001 (2016)
- [67] E. Berti, K. Yagi and N. Yunes, *Gen. Rel. Grav.* **50**, no. 4, 46 (2018)
- [68] E. Berti, K. Yagi, H. Yang and N. Yunes, *Gen. Rel. Grav.* **50**, no. 5, 49 (2018)
- [69] V. Cardoso, E. Franzin and P. Pani, *Phys. Rev. Lett.* **116**, no. 17, 171101 (2016) Erratum: [*Phys. Rev. Lett.* **117**, no. 8, 089902 (2016)]
- [70] V. Cardoso, S. Hopper, C. F. B. Macedo, C. Palenzuela and P. Pani, *Phys. Rev. D* **94**, no. 8, 084031 (2016).
- [71] V. Cardoso and P. Pani, *Nat. Astron.* **1**, no. 9, 586 (2017)
- [72] K. Akiyama *et al.* [Event Horizon Telescope Collaboration], *Astrophys. J.* **875**, no. 1, L6 (2019)
- [73] B. Kleihaus, J. Kunz and P. Kanti, *Phys. Lett. B* **804**, 135401 (2020)
- [74] P. V. P. Cunha, E. Berti and C. A. R. Herdeiro, *Phys. Rev. Lett.* **119**, no. 25, 251102 (2017)
- [75] J. Sakstein and B. Jain, *Phys. Rev. Lett.* **119**, no. 25, 251303 (2017)
- [76] I. Z. Fisher, *Zh. Eksp. Teor. Fiz.* **18**, 636 (1948) [gr-qc/9911008].
- [77] A. I. Janis, E. T. Newman and J. Winicour, *Phys. Rev. Lett.* **20** (1968) 878. doi:10.1103/PhysRevLett.20.878
- [78] M. Wyman, *Phys. Rev. D* **24** (1981) 839. doi:10.1103/PhysRevD.24.839
- [79] A. G. Agnese and M. La Camera, *Phys. Rev. D* **31** (1985) 1280. doi:10.1103/PhysRevD.31.1280
- [80] M. D. Roberts, *Gen. Rel. Grav.* **21** (1989) 907. doi:10.1007/BF00769864
- [81] V. P. Frolov, M. A. Markov and V. F. Mukhanov, *Phys. Rev. D* **41** (1990) 383.
- [82] E. I. Guendelman, *Int. J. Mod. Phys. D* **19**, 1357 (2010)
- [83] S. V. Chernov and V. I. Dokuchaev, *Class. Quant. Grav.* **25** (2008) 015004
- [84] V. I. Dokuchaev and S. V. Chernov, *JETP Lett.* **85** (2007) 595 [*Pisma Zh. Eksp. Teor. Fiz.* **85** (2007) 727]
- [85] V. Cardoso, L. C. B. Crispino, C. F. B. Macedo, H. Okawa and P. Pani, *Phys. Rev. D* **90**, no. 4, 044069 (2014)
- [86] J. Keir, *Class. Quant. Grav.* **33**, no. 13, 135009 (2016)
- [87] M. C. Teodoro, L. G. Collodel and J. Kunz, [arXiv:2003.05220 [astro-ph.HE]].
- [88] C. A. R. Herdeiro, J. M. S. Oliveira and E. Radu, *Eur. Phys. J. C* **80**, no.1, 23 (2020)